Prepared for submission to JHEP

Extract the energy scale of anomalous $\gamma\gamma \to W^+W^-$ scattering in the vector boson scattering process using artificial neural networks

Ji-Chong Yang Jin-Hua Chen Yu-Chen Guo

Department of Physics, Liaoning Normal University,

No. 850 Huanghe Road, Dalian 116029, P.R. China

E-mail: yangjichong@lnnu.edu.cn, cjh18241890611@163.com, ycguo@lnnu.edu.cn

Abstract: As a model independent approach to search for the signals of new physics (NP) beyond the Standard Model (SM), the SM effective field theory (SMEFT) draws a lot of attention recently. The energy scale of a process is an important parameter in the study of an EFT such as the SMEFT. However, for the processes at a hadron collider with neutrinos in the final states, the energy scales are difficult to reconstruct. In this paper, we study the energy scale of anomalous $\gamma\gamma \to W^+W^-$ scattering in the vector boson scattering (VBS) process $pp \to jj\ell^+\ell^-\nu\bar{\nu}$ at the large hadron collider (LHC) using artificial neural networks (ANNs). We find that the ANN is a powerful tool to reconstruct the energy scale of $\gamma\gamma \to W^+W^-$ scattering. The factors affecting the effects of ANNs are also studied. In addition, we make an attempt to interpret the ANN and arrive at an approximate formula which has only five fitting parameters and works much better than the approximation derived from kinematic analysis. With the help of ANN approach, the unitarity bound is applied as a cut on the energy scale of $\gamma\gamma \to W^+W^-$ scattering, which is found to has a significant suppressive effect on signal events. The sensitivity of the process $pp \to jj\ell^+\ell^-\nu\bar{\nu}$ to anomalous $\gamma\gamma WW$ couplings and the expected constraints on the coefficients at current and possible future LHC are also studied.

arXiv:2107.13624v3 [hep-ph] 20 Oct 2023

Contents

1 Introduction 1

2 A brief introduction of aQGCs 3

3 Approximation of the energy scale 5

4 Numerical results of the ANN 5
- 4.1 ANN approach 6
- 4.2 The information in the data-set 8
  - 4.2.1 Compare different sectors 9
  - 4.2.2 Compare different operators 10
  - 4.2.3 Compare different collision energies 10

5 Interpretation of the ANN 11

6 Expected constraints on the aQGCs 14
- 6.1 One ANN for all couplings 14
- 6.2 Signals and backgrounds 15
- 6.3 Unitarity bounds 18
- 6.4 Signal significance 19

7 Summary 22

1 Introduction

The Standard Model (SM) has proven to be very successful and accurate. Searching for new physics (NP) beyond the SM is one of the main goals of current and future colliders. Due to the lack of clear guidelines, a model independent approach to look for NP signals has gradually become popular, known as the SM effective field theory (SMEFT) [1–4]. It is assumed that energy scales of processes at current colliders are not large enough to directly produce the signals of NP particles. At low energies, the NP sector is decoupled, one can integrate out NP particles, then NP effects become new interactions of known particles, which are in the form of higher dimensional operators. Then, the SM can be extended as a low energy EFT of some unknown UV completion by adding those higher dimensional operators with small Wilson coefficients, result in a Lagrangian as

$$\mathcal{L}_{\text{SMEFT}} = \mathcal{L}_{SM} + \sum_i \frac{C_{6i}}{\Lambda^2}\mathcal{O}_{6i} + \sum_j \frac{C_{8j}}{\Lambda^4}\mathcal{O}_{8j} + \dots, \tag{1.1}$$

where $\mathcal{O}_{6i}$ and $\mathcal{O}_{8j}$ are dimension-6 and dimension-8 operators, C_{6i}/Λ^2 and C_{8j}/Λ^4 are corresponding Wilson coefficients, Λ is the energy scale of NP. In Eq. (1.1), we have neglected the odd-dimensional operators which violate the lepton number conservation.

To investigate an EFT, the energy scale is an important parameter, because the Wilson coefficients are functions of energy scales. It has been suggested that, in experiments the constraints on the Wilson coefficients of higher dimensional operators should be given as functions of energy scales [5]. Meanwhile, there are theoretical constraints such as the unitarity bounds [6–10] which are also functions of energy scales. In conclusion, the reconstruction of the center-of-mass (c.m.) energy is an important task in phenomenological studies of the SMEFT.

At a proton-proton (pp) collider such as the Large Hadron Collider (LHC), due to the parton distribution function (PDF), the c.m. energy can only be reconstructed by using the information in the final states. This poses difficulties for processes whose final states contain neutrinos. For example, for the vector boson scattering (VBS) process $pp \to jj\gamma W$, in order to study the unitarity bounds of anomalous quartic couplings (aQGCs), one needs to reconstruct the c.m. energy of subprocess $\gamma(Z)W \to \gamma W$ subjected to a delicate kinematic analysis and approximation [11]. Another example is the process $pp \to WW$, where the study of validity of the SMEFT has also encountered great difficulties due to the neutrinos in the final state [12, 13].

There is a similar problem in the studies of processes containing vector bosons at the LHC. The longitudinal polarized vector bosons are related to the symmetry broken and the Higgs mechanism, therefore draws a lot of attention [14–19]. The polarization of a vector boson can be inferred by the momentum of the daughter charged lepton in the rest-frame of the vector boson, the so called helicity frame [20]. However, the momentum of the $W^{\pm}$ boson is difficult to reconstruct due the neutrino, as a result, it is difficult to boost the charged lepton to the rest frame of the W boson, which is one of the reasons that the polarization of a W boson is difficult to determinate. In response to the problems in determining the polarizations, a novel approach has been introduced into high energy physics (HEP). It has been shown that, the artificial neural network (ANN) can be very powerful in determining the polarizations of W, Z bosons [21–23] and τ lepton [24]. The ANN approach is one of the machine learning methods, which have been widely used in HEP, and are being developed rapidly in recent years [25–34].

In this paper, we study the aQGCs induced by dimension-8 operators [35, 36] in the process $pp \to jjW^+W^-$ with leptonic decays of $W^{\pm}$ bosons. The aQGCs can be contributed by a lot of NP models [37–47], and has been studied intensively [48–53]. Dimension-6 operators cannot contribute to aQGCs while leaving anomalous triple gauge couplings (aTGCs) along [50], therefore we concentrate on the dimension-8 operators. A recent study shows that the existence of dimension-8 operators is necessary as long as the dimension-6 operators exist in the convex geometry point of view to the SMEFT space [54]. Besides, there are cases that the contributions from dimension-6 operators are absent [37, 38, 55–59]. Moreover, aQGCs can lead to richer helicity combinations than dimension-6 aTGCs [60]. Apart from that, aQGCs can be generated by tree diagrams while aTGCs are generated by loop diagrams [61], therefore the possibility exists that the signals of dimension-8 aQGCs

are more significant than the dimension-6 aTGCs. Consequently, while the SMEFT has mainly been applied with dimension-6 operators, recently the study of dimension-8 operators has gradually received much attention [35, 36, 55, 62]. The most sensitive processes for aQGCs are the VBS processes [63]. The VBS processes have been extensively studied by both the ATLAS and the CMS groups [60, 64–78], and will continue to draw attentions with future runs of the LHC. The evidence of exclusive or quasi-exclusive $\gamma\gamma \to W^+W^-$ process has been found [79]. The next-to-leading order QCD corrections to the process $pp \to W^+W^-jj$ have been computed [80], and the K factor is found to be close to one ($K \approx 0.98$). As introduced, to study the dimension-8 operators, the two neutrinos in the final state will cause difficulties. However, these difficulties just provide a good test for the ANN approach. We use the ANN approach to study the process $pp \to jj\ell^+\ell^-\nu\bar{\nu}$ with the focus on the reconstruction of the energy scale of the $\gamma\gamma \to W^+W^-$ subprocess. We discuss the justification of using ANN to study the energy of the subprocess, and show that the ANN can achieve better results than kinematic analysis. An interpretation of the ANN is discussed, which indicates that the ANN can be approximated by a function of three variables and contains five fitting parameters. The unitarity bounds and the signal significances of the aQGCs are also studied in this paper.

The remainder of the paper is organized as follows, in Sec. 2 we briefly introduce the aQGCs; in Sec. 3 the kinematic analysis is presented; the numerical results of the ANN approach is shown in Sec. 4; an interpretation of the ANN is presented in Sec. 5; in Sec. 6, we use the results of ANN to study the unitarity bounds and signal significances of aQGCs; Sec. 7 is a summary.

2 A brief introduction of aQGCs

In this section, we briefly introduce the dimension-8 operators contributing to the aQGCs frequently used in experiments. The Lagrangian relevant to the process $\gamma\gamma \to W^+W^-$ is $\mathcal{L}_{\rm aQGC} = \sum_i (f_{S_i}/\Lambda^4) O_{S,i} + \sum_j (f_{M_j}/\Lambda^4) O_{M,j} + \sum_k (f_{T_k}/\Lambda^4) O_{T,k}$ with [35, 36]

$$
\begin{aligned}
O_{S,0} &= \left[(D_\mu\Phi)^\dagger D_\nu\Phi\right] \times \left[(D^\mu\Phi)^\dagger D^\nu\Phi\right], & O_{T,0} &= \mathrm{Tr}\left[\widehat{W}_{\mu\nu}\widehat{W}^{\mu\nu}\right] \times \mathrm{Tr}\left[\widehat{W}_{\alpha\beta}\widehat{W}^{\alpha\beta}\right],\\
O_{S,1} &= \left[(D_\mu\Phi)^\dagger D_\mu\Phi\right] \times \left[(D^\nu\Phi)^\dagger D^\nu\Phi\right], & O_{T,1} &= \mathrm{Tr}\left[\widehat{W}_{\alpha\nu}\widehat{W}^{\mu\beta}\right] \times \mathrm{Tr}\left[\widehat{W}_{\mu\beta}\widehat{W}^{\alpha\nu}\right],\\
O_{S,2} &= \left[(D_\mu\Phi)^\dagger D_\nu\Phi\right] \times \left[(D^\nu\Phi)^\dagger D^\mu\Phi\right], & O_{T,2} &= \mathrm{Tr}\left[\widehat{W}_{\alpha\mu}\widehat{W}^{\mu\beta}\right] \times \mathrm{Tr}\left[\widehat{W}_{\beta\nu}\widehat{W}^{\nu\alpha}\right],\\
O_{M,0} &= \mathrm{Tr}\left[\widehat{\mathrm{W}}_{\mu\nu}\widehat{\mathrm{W}}^{\mu\nu}\right] \times \left[\left(D^\beta\Phi\right)^\dagger D^\beta\Phi\right], & O_{T,5} &= \mathrm{Tr}\left[\widehat{W}_{\mu\nu}\widehat{W}^{\mu\nu}\right] \times B_{\alpha\beta}B^{\alpha\beta},\\
O_{M,1} &= \mathrm{Tr}\left[\widehat{\mathrm{W}}_{\mu\nu}\widehat{\mathrm{W}}^{\nu\beta}\right] \times \left[\left(D^\beta\Phi\right)^\dagger D^\mu\Phi\right], & O_{T,6} &= \mathrm{Tr}\left[\widehat{W}_{\alpha\nu}\widehat{W}^{\mu\beta}\right] \times B_{\mu\beta}B^{\alpha\nu},\\
O_{M,2} &= \left[B_{\mu\nu}B^{\mu\nu}\right] \times \left[\left(D^\beta\Phi\right)^\dagger D^\beta\Phi\right], & O_{T,7} &= \mathrm{Tr}\left[\widehat{W}_{\alpha\mu}\widehat{W}^{\mu\beta}\right] \times B_{\beta\nu}B^{\nu\alpha},\\
O_{M,3} &= \left[B_{\mu\nu}B^{\nu\beta}\right] \times \left[\left(D^\beta\Phi\right)^\dagger D^\mu\Phi\right], & O_{T,8} &= B_{\mu\nu}B^{\mu\nu} \times B_{\alpha\beta}B^{\alpha\beta},\\
O_{M,4} &= \left[(D_\mu\Phi)^\dagger \widehat{W}_{\beta\nu} D^\mu\Phi\right] \times B^{\beta\nu}, & O_{T,9} &= B_{\alpha\mu}B^{\mu\beta} \times B_{\beta\nu}B^{\nu\alpha},\\
O_{M,5} &= \left[(D_\mu\Phi)^\dagger \widehat{W}_{\beta\nu} D_\nu\Phi\right] \times B^{\beta\mu} + h.c., & & \\
O_{M,7} &= (D_\mu\Phi)^\dagger \widehat{W}_{\beta\nu}\widehat{W}_{\beta\mu} D_\nu\Phi, & &
\end{aligned}
\tag{2.1}
$$

where Φ is the SM Higgs doublet, $\widehat{W} \equiv \vec{\sigma} \cdot \vec{W}/2$ with σ being the Pauli matrices and $\vec{W} \equiv \{W^1, W^2, W^3\}$. The $O_{M_{0,1,2,3,4,5,7}}$ and $O_{T_{0,1,2,5,6,7}}$ operators can contribute to five anomalous $\gamma\gamma WW$ couplings, which can be written as $\mathcal{L}_{\gamma\gamma WW} = \sum_{i=0}^{4} \alpha_i V_i$ with [52]

$$\begin{aligned} V_0 &= F_{\mu\nu}F^{\mu\nu}W^{+\alpha}W^{-}_{\alpha}, \quad V_1 = F_{\mu\nu}F^{\mu\alpha}W^{+\nu}W^{-}_{\alpha}, \\ V_2 &= F_{\mu\nu}F^{\mu\nu}W^{+}_{\alpha\beta}W^{-\alpha\beta}, \; V_3 = F_{\mu\nu}F^{\nu\alpha}W^{+}_{\alpha\beta}W^{-\beta\mu}, \\ V_4 &= F_{\mu\nu}F^{\alpha\beta}W^{+\mu\nu}W^{-}_{\alpha\beta}, \end{aligned} \tag{2.2}$$

where $W^{\pm}_{\mu\nu} \equiv \partial_\mu W^{\pm}_{\nu} - \partial_\nu W^{\pm}_{\mu}$. The coefficients of the couplings can be related to the coefficients of the operators as

$$\begin{aligned} &\alpha_0 = \tfrac{e^2v^2}{8\Lambda^4}\left(f_{M_0} + \tfrac{c_W}{s_W} f_{M_4} + 2\tfrac{c_W^2}{s_W^2} f_{M_2}\right), \; \alpha_1 = \tfrac{e^2v^2}{8\Lambda^4}\left(\tfrac{1}{2} f_{M_7} + 2\tfrac{c_W}{s_W} f_{M_5} - f_{M_1} - 2\tfrac{c_W^2}{s_W^2} f_{M_3}\right), \\ &\alpha_2 = \tfrac{1}{\Lambda^4}\left(s_W^2 f_{T_0} + c_W^2 f_{T_5}\right), \qquad \alpha_3 = \tfrac{1}{\Lambda^4}\left(s_W^2 f_{T_2} + c_W^2 f_{T_7}\right), \\ &\alpha_4 = \tfrac{1}{\Lambda^4}\left(s_W^2 f_{T_1} + c_W^2 f_{T_6}\right). \end{aligned} \tag{2.3}$$

Because each dimension-8 operator contributes to only one vertex, and the constraints on the dimension-8 operators are obtained by assuming one operator at a time in experiments, the constraints on α_i can be derived by the constraints on dimension-8 operators [52] which are listed in Table 1. For simplicity, we concentrate on these five couplings in this paper.

vertex	constraint	coefficient	constraint
$\alpha_0(\text{TeV}^{-2})$	$[-0.013, 0.013]$	$f_{M_2}/\Lambda^4\ (\text{TeV}^{-4})$	$[-2.8, 2.8]$
$\alpha_1(\text{TeV}^{-2})$	$[-0.021, 0.021]$	$f_{M_5}/\Lambda^4\ (\text{TeV}^{-4})$	$[-8.3, 8.3]$
$\alpha_2(\text{TeV}^{-4})$	$[-0.38, 0.38]$	$f_{T_5}/\Lambda^4\ (\text{TeV}^{-4})$	$[-0.5, 0.5]$
$\alpha_3(\text{TeV}^{-4})$	$[-0.69, 0.69]$	$f_{T_7}/\Lambda^4\ (\text{TeV}^{-4})$	$[-0.9, 0.9]$
$\alpha_4(\text{TeV}^{-4})$	$[-0.31, 0.31]$	$f_{T_6}/\Lambda^4\ (\text{TeV}^{-4})$	$[-0.4, 0.4]$

Table 1: The constraints on anomalous $\gamma\gamma WW$ couplings and the corresponding limits on the dimension-8 operators at 95% CL [75].

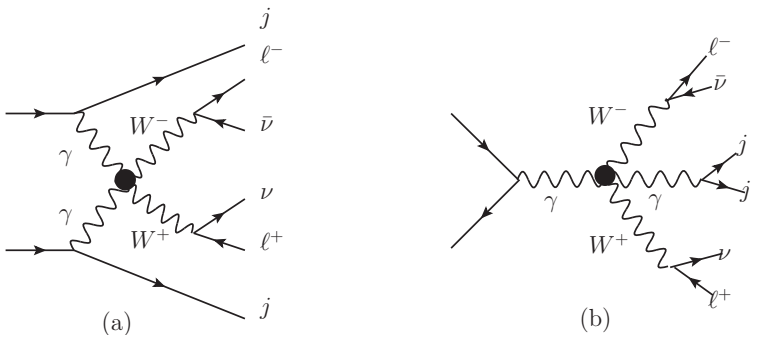


Figure 1: The Feynman diagrams of the contributions from anomalous $\gamma\gamma WW$ couplings to the process $pp \to jj\ell^+\ell^-\nu\bar{\nu}$.

The process $pp \to W^+W^-jj$ can be affected by the anomalous $\gamma\gamma WW$ couplings as shown in Fig. 1. The contribution from the tri-boson channel shown in Fig. 1. (b) was

found to be about three orders of magnitude smaller compared with the VBS contribution in Fig. 1. (a) [52], therefore in the following discussions we concentrate on the effect of the VBS contribution. Moreover, we only consider the leptonic decays of the $W^{\pm}$ bosons, and focus on the process $pp \to \ell^+\ell^-\bar{\nu}\nu jj$ at $\sqrt{s} = 13$ TeV, with $\ell = e, \mu$. To distinguish, the s of the subprocess $\gamma\gamma \to W^+W^-$ is denoted as $\hat{s}$.

3 Approximation of the energy scale

A prerequisite for using an ANN to mine information is that the information to be mined actually exists. This is extremely important because the ANN is considered to be a 'black box'. To demonstrate that the $\hat{s}$ can be approximately reconstructed, and also as a comparison, we briefly introduce the method for estimating $\hat{s}$ in Ref. [52]. Assuming the $W^{\pm}$ bosons are energetic and neglecting the $\mathcal{O}(M_W/\sqrt{\hat{s}})$ contributions, the leptons can be viewed as approximately collinear to the neutrinos, i.e., with u and v the coefficients to be determined, the momenta of the neutrinos can be related to the momenta of the charged leptons as $\mathbf{p}^{\nu} \approx u\mathbf{p}^{\ell^+}$ and $\mathbf{p}^{\bar{\nu}} \approx v\mathbf{p}^{\ell^-}$, which lead to the equations

$$\mathbf{p}_x^{\text{miss}} = u\mathbf{p}_x^{\ell^+} + v\mathbf{p}_x^{\ell^-}, \quad \mathbf{p}_y^{\text{miss}} = u\mathbf{p}_y^{\ell^+} + v\mathbf{p}_y^{\ell^-}, \tag{3.1}$$

by which u and v can be solved and then $\hat{s}$ can be reconstructed. The result is

$$\begin{aligned} \hat{s}_{\text{ap}} = &\left((1+|u|)E^{\ell^+} + (1+|v|)E^{\ell^-}\right)^2 \\ &- \left((1+u)\mathbf{p}_z^{\ell^+} + (1+v)\mathbf{p}_z^{\ell^-}\right)^2 - \left|\sum_{\pm} \mathbf{p}_T^{\ell^\pm} + \mathbf{p}_T^{\text{miss}}\right|^2, \end{aligned} \tag{3.2}$$

where

$$u = \frac{1}{\kappa}\left(\mathbf{p}_y^{\text{miss}}\mathbf{p}_x^{\ell^-} - \mathbf{p}_x^{\text{miss}}\mathbf{p}_y^{\ell^-}\right), \quad v = -\frac{1}{\kappa}\left(\mathbf{p}_y^{\text{miss}}\mathbf{p}_x^{\ell^+} - \mathbf{p}_x^{\text{miss}}\mathbf{p}_y^{\ell^+}\right), \tag{3.3}$$

with

$$\kappa = \mathbf{p}_y^{\ell^+}\mathbf{p}_x^{\ell^-} - \mathbf{p}_x^{\ell^+}\mathbf{p}_y^{\ell^-}. \tag{3.4}$$

This approximation is based on the assumption that $W^{\pm}$ bosons are energetic, which is supported by the fact that the $\hat{s}$ are large for the signal events induced by aQGCs. However, when $\hat{s}$ is large, the charged leptons are approximately back-to-back, and the two equations in Eq. (3.1) will degenerate when charged leptons are exactly back-to-back. In other words, for most events induced by aQGCs, the κ are very small. When κ is close to zero, it will amplify the errors in numerator, resulting in an inaccurate approximation.

Since approximations exist, using an ANN to reconstruct $\hat{s}$ is nothing but to look for a better approximation. The ANN is good at looking for approximations and finding patterns in complex relationships, and therefore has the potential to yield better results.

4 Numerical results of the ANN

In this section we use the ANN approach to reconstruct $\hat{s}$. To train the ANN, we use the Monte-Carlo (MC) simulation to generate the data-sets. We take the contributions

from both diagrams of Fig. 1 as the signal because they both signal the existence of the aQGCs. As explained, the effect of Fig. 1. (b) is negligible compared with Fig. 1. (a). In the following discussions, we concentrate on Fig. 1. (a) and neglect the effect of Fig. 1. (b), despite that the data-sets are generated with both diagrams included.

The signal events are generated by using `MadGraph5_aMC@NLO` [81, 82], with a parton shower using `Pythia82` [83]. The PDF is `NNPDF2.3` [84]. A CMS-like detector simulation is applied using `Delphes` [85]. The events are generated assuming one operator at a time, and using the largest coefficients listed in Table 1.

The signal of the VBS process is characterized by two quark jets, events are thus required to have at least 2 jets and two opposite sign charged leptons. The dominant background is the process $pp \to t\bar{t} + Nj$ with $t \to W^+b$ ($\bar{t} \to W^+\bar{b}$) and with b-jet mistagged. To reduce this background, we also require $N_j \leq 5$. In the following, the results are established after the lepton number cut and jet number cut $N_\ell = 2$ and $2 \leq N_j \leq 5$. To train the ANN, we generate 10^6 events to build the training data-set, and another 10^6 events to build the validation data-set for each anomalous $\gamma\gamma WW$ coupling. After the requirement on the numbers of leptons and jets, there are about 6×10^5 events in each data-set.

Before the detector simulation, the $\hat{s}$ can be obtained, which is denoted as $\hat{s}_{\rm tr}$. Each event corresponds to an element in the data-set consists of 19 variables. For each event, an 18 dimensional vector provides as the input to the ANN, which consists of 18 variables. They are the components of the 4-momenta of the two hardest jets, the 4-momenta of the two hardest opposite signed charged leptons and the components of the transverse missing momentum. The output of the ANN corresponds to $\hat{s}$. The true labels are the 19-th variables of the elements in the data-sets which are $\hat{s}_{\rm tr}$ of the events.

In this section, we mainly focus on the contribution of V_0 vertex. It has been found that the process $pp \to jj\ell^+\ell^-\nu\bar{\nu}$ is insensitive to the V_4 vertex [52], we do not study V_4 in this paper.

4.1 ANN approach

ANN is a mathematical model to simulate the complex neural system of a human brain, and it is also an information processing system for large-scale distributed parallel information processing [86]. The ANN is good at finding the complex mathematical mapping relationships between input and output, it could be utilized to unveil hidden information in the final states. The mapping relationship is determined by the number of interconnected nodes and their connection modes. In this paper, we use a dense connected ANN.

An ANN is composed with one or more hidden layers and an output layer. Denoting x^i_j as neurons in the i-th layer, where $x^1_{1\leq j\leq n_1}$ are input neurons, $x^{2\leq i\leq l-1}_{1\leq j\leq n_i}$ are in hidden layers and x^l_1 is the output neuron, the ANN can be depicted in Fig. 2.

Without causing ambiguity, the value at a neuron takes the same notation x^i_j. $x^{i+1}_{j'}$ can be related with x^i_j as

$$x^{i+1}_{j'} = f^{i+1}\left(\sum_j \omega^{i+1}_{jj'} x^i_j + b^{i+1}_{j'}\right) \tag{4.1}$$

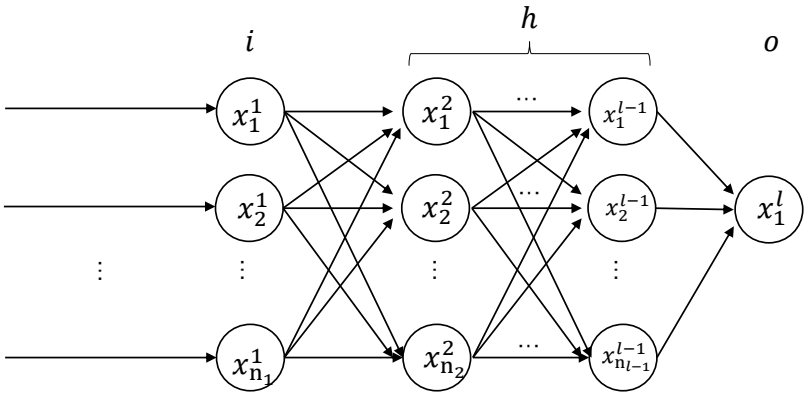


Figure 2: The architecture of an ANN used in this paper. 'i', 'h' and 'o' stand for input layer, hidden layer and output layer, respectively. l is the number of layers and n_i is the number of neurons in the i-th layer.

where $\omega_{jj'}^{i+1}$ are elements of a weight matrix W^{i+1}, $b_{j'}^{i+1}$ are components of a bias vector, and f^{i+1} is an activate function. The activation functions for the hidden layers are chosen as the parametric rectified linear unit (PReLU) function [87] defined as

$$f(x) = \begin{cases} x, & x \geq 0; \\ \alpha x, & x < 0, \end{cases} \tag{4.2}$$

where α's are trainable parameters. For the output layer, no activation function (i.e., linear activation function) is used. In this paper, without further specification we use $l = 10$, $n_{10>l>1} = 32$, n_1 is as same as the dimension of input data and $n_{10} = 1$ for the output layer. The training data-sets are normalized using the z-score standardization, i.e., denoting v_i as the i-th variable of one of the elements in the data-sets, v_i' is used instead of v_i which is defined as $v_i' = (v_i - \bar{v_i})/\sigma_{v_i}$, where $\bar{v_i}$ and σ_{v_i} are the mean value and the standard deviation of all i-th variables of the elements in the data-sets.

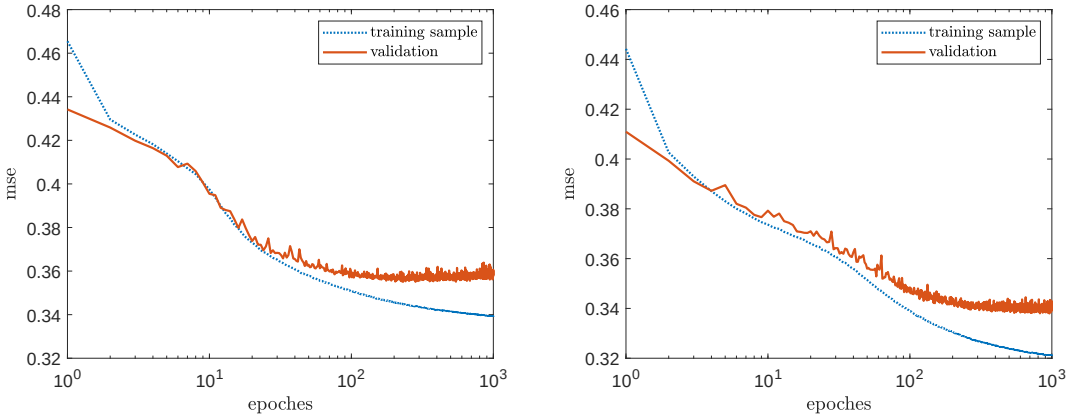


Figure 3: The learning curves of the ANNs trained with $V_{0,2}$ data-sets.

The architecture is built using `Keras` with a `TensorFlow` [88] backend. The data

preparation is performed by `MLAnalysis` [89]. The learning curves of the ANNs for V_0 and V_2 are shown in Fig. 3. Note that the label is also standardized, therefore the mean squared error (mse) is dimensionless. From Fig. 3, we find that the mse stopped to decrease at about 150 epoches for $V_{0,1}$ vertices, and at about 300 epoches for $V_{2,3}$ vertices. To avoid overfitting, we stop the training at 150 epoches for $V_{0,1}$ vertices, and at 300 epoches for $V_{2,3}$ vertices. Note that the $V_{0,1}$ vertices are from O_{M_i} operators and $V_{2,3}$ vertices are from the O_{T_i} operators, it is interesting that the ANNs are more difficult to train with the signal events induced by O_{T_i} operators.

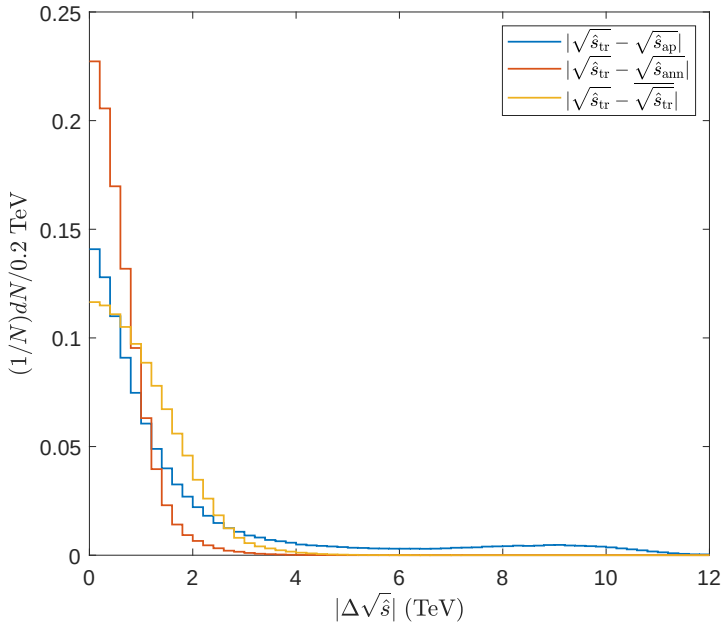


Figure 4: The normalized distributions of $|\Delta\sqrt{\hat{s}}|$ for $\overline{\sqrt{\hat{s}}}$, $\hat{s}_{\rm ap}$ and $\hat{s}_{\rm ann}$.

Denoting $\hat{s}_{\rm ann}$ as the $\hat{s}$ predicted by the ANN. For the validation data-set, the normalized distributions of $|\sqrt{\hat{s}_{\rm tr}} - \overline{\sqrt{\hat{s}_{\rm tr}}}|$, $|\sqrt{\hat{s}_{\rm tr}} - \sqrt{\hat{s}_{\rm ap}}|$ and $|\sqrt{\hat{s}_{\rm tr}} - \sqrt{\hat{s}_{\rm ann}}|$ are shown in Fig. 4, where $\overline{\sqrt{\hat{s}_{\rm tr}}}$ is the mean value of $\sqrt{\hat{s}_{\rm tr}}$. One can see that the deviation of $\sqrt{\hat{s}_{\rm ap}}$ from $\sqrt{\hat{s}_{\rm tr}}$ is smaller than using $\overline{\sqrt{\hat{s}_{\rm tr}}}$ as an approximation. On the other hand, the result of the ANN is much better than the approximation derived from the kinematical analysis.

4.2 The information in the data-set

It has been shown that the ANN can reconstruct $\hat{s}$ much better than the kinematical analysis. In this subsection, we investigate how the performances of the ANNs are affected by different factors. Specifically, we are interested in where does the information to reconstruct $\hat{s}$ contained in. To answer this question, we pay particular attention to the information that is not used by the approximation in Eq. (3.2). In this subsection, the epoches are determined similarly as the previous subsection.

4.2.1 Compare different sectors

The approximation in Eq. (3.2) does not use the momenta of jets which are difficult to be made use of. To investigate how the results are affected by the information contained in jets, charged leptons and missing momentum, we divide the input data into 3 sectors. We denote $\hat{s}_{2\mathrm{lm}}$ as the $\hat{s}$ predicted by the ANN trained with the data-set consists of the components of the 4-momenta of the two hardest opposite signed charged leptons and the transverse missing momentum, $\hat{s}_{2\mathrm{jm}}$ as the result of the ANN trained with the data-set consists of the components of the 4-momenta of the two hardest jets and the transverse missing momentum, $\hat{s}_{2\mathrm{j2l}}$ as the result of the ANN trained with the data-set consists of the components of the 4-momenta of the two hardest jets and the 4-momenta of the two hardest opposite signed charged leptons, $\hat{s}_{2\mathrm{j}}$ as the result of the ANN trained with the data-set consists of the components of the 4-momenta of the two hardest jets, $\hat{s}_{2\mathrm{l}}$ as the result of the ANN trained with the data-set consists of the components of the 4-momenta of the two hardest opposite signed charged leptons, $\hat{s}_{\mathrm{m}}$ as the result of the ANN trained with the data-set consists of the components of the transverse missing momentum, respectively.

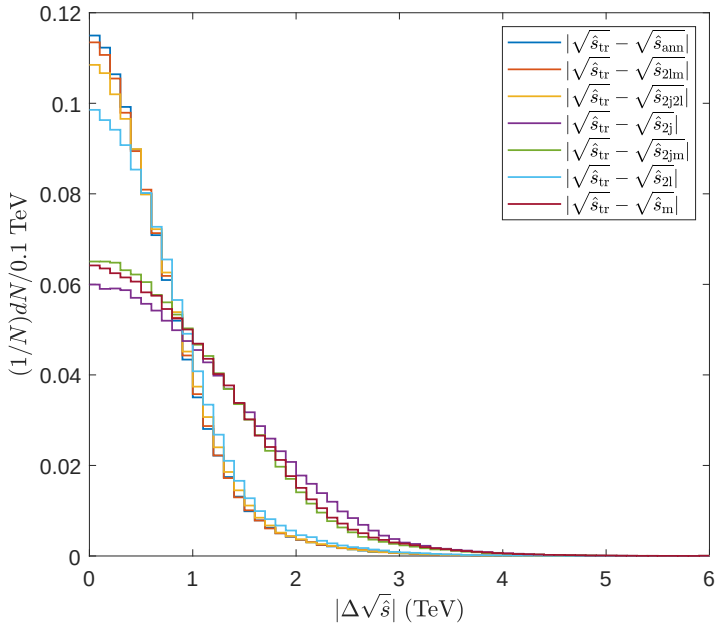


Figure 5: The normalized distributions of $|\Delta\sqrt{\hat{s}}|$ for $\hat{s}_{\mathrm{ann}}$, $\hat{s}_{2\mathrm{lm}}$, $\hat{s}_{2\mathrm{jm}}$, $\hat{s}_{2\mathrm{j2l}}$, $\hat{s}_{2\mathrm{l}}$, $\hat{s}_{2\mathrm{j}}$ and $\hat{s}_{\mathrm{m}}$.

The normalized distributions of $|\Delta\sqrt{\hat{s}}|$ are shown in Fig. 5. From the distributions we find that the importance of different sectors can be ordered as $p^{\ell^\pm} > \mathbf{p}_T^{\mathrm{miss}} > p^{\mathrm{jet}}$. Indeed, the ANN trained with the data-set including the momenta of jets can produce slightly more precise results. Nevertheless, the effect brought about by jets is small and is not the main reason why ANNs are more accurate.

4.2.2 Compare different operators

Except for assuming the events are induced by aQGCs, the approximation in Eq. (3.2) does not use any other information about the anomalous couplings. In the approximation, the formula to estimate $\sqrt{\hat{s}}$ is same for all couplings. Meanwhile, using the ANN approach, we can train the ANNs by using data-sets consist of signal events from different couplings. In this way we can investigate whether the distinction between couplings is important for the reconstruction of $\sqrt{\hat{s}}$.

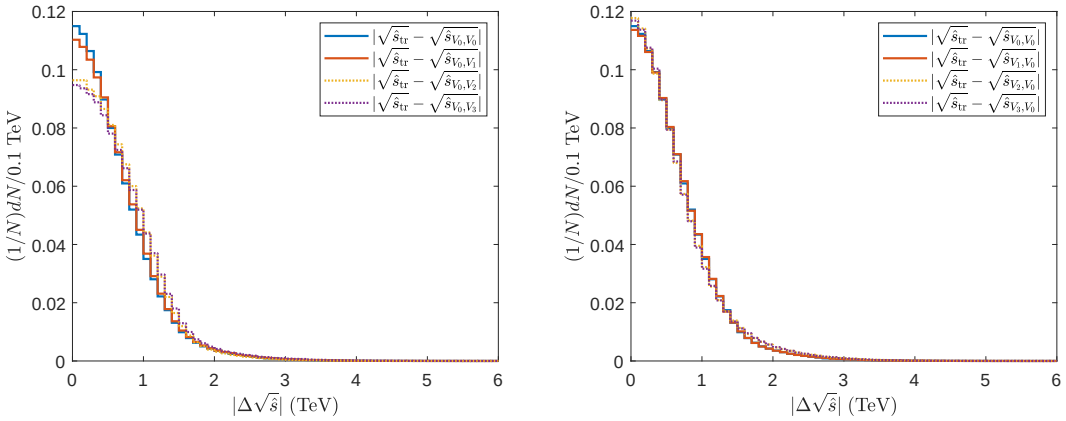


Figure 6: The normalized distributions of $|\Delta\sqrt{\hat{s}}|$ for $\hat{s}_{V_0,V_i}$ and $\hat{s}_{V_i,V_0}$. Note that $\hat{s}_{V_0,V_0}$ is the $\hat{s}_{\text{ann}}$ shown in Figs. 4 and 5.

Denoting the $\hat{s}_{V_i,V_j}$ as the predicted $\hat{s}$ of the events in a V_j validation data-set but predicted by the ANN trained with the V_i training data-set. The results of $\hat{s}_{V_0,V_i}$ and $\hat{s}_{V_i,V_0}$ are shown in Fig. 6. Again, the difference between O_{M_i} operators and O_{T_i} operators can be found from the results of $\hat{s}_{V_0,V_i}$. From the results of $\hat{s}_{V_i,V_0}$, it can be seen that the predictive powers of the ANNs trained using different data-sets are about the same for signal events of V_0 vertex. In fact, the ANN trained with V_3 training data-set is slightly more accurate than the ANN trained with V_0 training data-set in predicting the $\hat{s}$ of the V_0 validation data-set. Therefore we conclude that the information about different couplings is not made use of. The difference in the distributions of $|\sqrt{\hat{s}_{\text{tr}}} - \sqrt{\hat{s}_{V_0,V_i}}|$ is just another evidence that, from the perspectives of the ANNs the signal events induced by O_{T_i} operators are more difficult to learn.

4.2.3 Compare different collision energies

The approximation in Eq. (3.2) assumes that the $\hat{s}$ is large, however it does not use the information of collision energy $\sqrt{s} = 13$ TeV. To investigate whether this information is made use of, we prepare three training data-sets, which are the signal events of V_0 generated at $\sqrt{s} = 12, 13$ and 14 TeV. $\hat{s}$ of the events in the $\sqrt{s} = 13$ TeV V_0 validation data-set are predicted by the ANNs trained with the $\sqrt{s} = 12, 13$ and 14 TeV training data-sets, which are denoted as $\hat{s}_{12,13,14}$, respectively. The normalized distributions of $|\Delta\sqrt{\hat{s}_{12,13,14}}|$ are shown in Fig. 7.

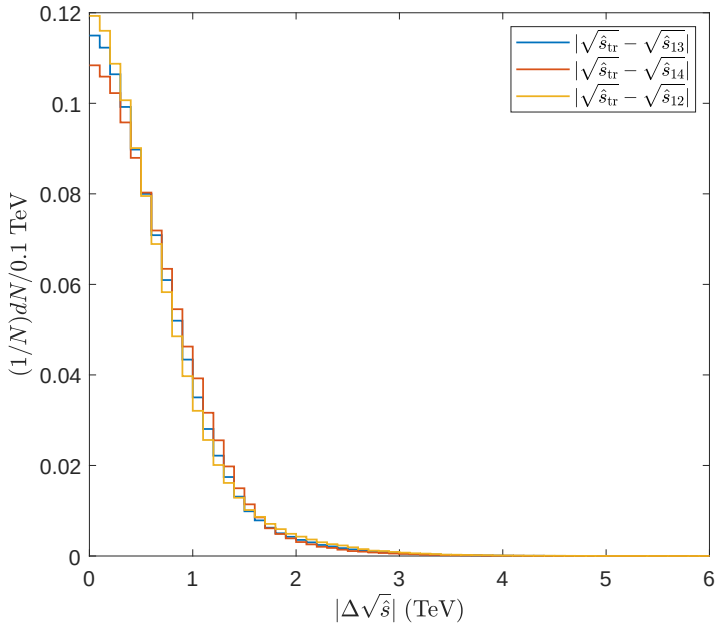


Figure 7: The normalized distributions of $\Delta\sqrt{\hat{s}}$ for $\hat{s}_{12,13,14}$. Note that $\hat{s}_{13}$ is the $\hat{s}_{\rm ann}$ shown in Figs. 4 and 5.

It can be seen from Fig. 7 that the results are close to each other, indicating that the $\sqrt{s}$ was also hardly used by the ANNs. It is interesting to notice that the ANN trained with the $\sqrt{s} = 12$ TeV training data-set can make even better prediction on the $\sqrt{s} = 13$ TeV validation data-set than the ANN trained with the $\sqrt{s} = 13$ TeV training data-set. In fact, the learning curve for the $\sqrt{s} = 12$ TeV training data-set converges slower than the case of 13 TeV. We speculate that, the ANN trained with the $\sqrt{s} = 12$ TeV data-set works better because the 12 TeV data-set is more difficult to train.

5 Interpretation of the ANN

To investigate how the $\sqrt{\hat{s}}$ is predicted by the ANNs, in this section, the implicity relation between $\sqrt{\hat{s}}$ and the inputs concealed in an ANN is investigated. Since the accuracy of the ANN trained with only 4-momenta of charged leptons has been able to achieve almost the best accuracy, for simplicity, we focus on the ANN trained with only 4-momenta of the charged leptons.

Once the ANN is trained, we can input arbitrary 4-momenta of the charged leptons to study the relationship between $\hat{s}$ and the 4-momenta. In this procedure, one can have a control on the variables, i.e., keep some variables constant and then change the others. In contrast, using M.C. simulation for such a study is difficult because the 4-momenta of charged leptons are generated according to the probability density and therefore are not arbitrary.

One of the reasons the ANN is called a 'black box' is that, although the ANN has an analytic expression, this expression is very complex and it is difficult to read the physics behind this expression. Another motivation of this section is to find a more understandable expression. In addition, this procedure can also be seen as a method to use the ANN to find an approximate formula.

We define $\hat{\theta}_{\ell^\pm} = \pi/2 - |\beta|$ where β is the angle between $\mathbf{p}^{\ell^\pm}$ and the $\mathbf{xy}$-plane, and therefore $\hat{\theta}_{\ell^\pm}$ is the zenith angle $\theta_{\ell^\pm}$ of a charged lepton when $\theta_{\ell^\pm} < \pi/2$ and $\pi - \theta_{\ell^\pm}$ when $\theta_{\ell^\pm} > \pi/2$, satisfying $0 \leq \hat{\theta}_{\ell^\pm} \leq \pi/2$. For the V_0 training data-set, we find the mean values are $\bar{E}_{\ell^+} \approx \bar{E}_{\ell^+} \approx 0.915 = \bar{E}$ and $\bar{\hat{\theta}}_{\ell^+} \approx \bar{\hat{\theta}}_{\ell^-} \approx 0.98 = \bar{\hat{\theta}}$.

Firstly, we use a pair of massless leptons with zero azimuth angles (denoted as $\phi_{\ell^\pm}$) and with $E_{\ell^\pm} = \bar{E}$. The 4-momenta are set as

$$\begin{aligned} p^{\ell^+} &= \bar{E}\,(1, \sin(\theta_{\ell^+}), 0, \cos(\theta_{\ell^+}))\,, \\ p^{\ell^-} &= \bar{E}\,(1, \sin(\theta_{\ell^-}), 0, \cos(\theta_{\ell^-}))\,, \end{aligned} \tag{5.1}$$

where θ_{ℓ^+} and θ_{ℓ^-} are free parameters. The $\sqrt{\hat{s}}$ as a function of θ_{ℓ^+} and θ_{ℓ^-} predicted by the ANN is shown in the left panel of Fig. 8. We find that the $\sqrt{\hat{s}}$ can be well fitted as $a_1 + a_2\cos(\theta_{\ell^+} - \theta_{\ell^-})$, which is shown as the curved surface.

Moreover, we also investigate how $\sqrt{\hat{s}}$ depends on E_{ℓ^+} and E_{ℓ^-}. For this purpose, we introduce a pair of back-to-back massless leptons with the directions of $\mathbf{p}^{\ell^+}$ and $\mathbf{p}^{\ell^-}$ fixed, i.e., we use the following 4-momenta

$$\begin{aligned} p^{\ell^+} &= E_{\ell^+}\left(1, \sin(\bar{\hat{\theta}}), 0, \cos(\bar{\hat{\theta}})\right), \\ p^{\ell^-} &= E_{\ell^-}\left(1, -\sin(\bar{\hat{\theta}}), 0, -\cos(\bar{\hat{\theta}})\right), \end{aligned} \tag{5.2}$$

where E_{ℓ^+} and E_{ℓ^-} are free parameters. The $\sqrt{\hat{s}}$ as a function of E_{ℓ^+} and E_{ℓ^-} predicted by the ANN is shown in the right panel of Fig. 8. We find that the $\sqrt{\hat{s}}$ can be well fitted as $b_1 + b_2(E_{\ell^+} + E_{\ell^-}) + b_3 E_{\ell^+} E_{\ell^-}$, which is shown as the curved surface.

Denoting the angle between the momenta of $\ell^\pm$ as $\theta_{\ell\ell}$, the relation between $\sqrt{\hat{s}}$ and $\theta_{\ell\ell}$ is investigated. In this case, we use $p^{\ell^+} = \bar{E}\left(1, \sin(\bar{\hat{\theta}}), 0, \cos(\bar{\hat{\theta}})\right)$, and let $\mathbf{p}_{\ell^-}$ be on the surface of a cone whose central axis is $\mathbf{p}^{\ell^+}$, with $E_{\ell^-} = \bar{E}$. The $\mathbf{p}^{\ell^+}$ and $\mathbf{p}^{\ell^-}$ are depicted in the left panel of Fig. 9 where the definition of $\phi_{\ell\ell}$ is shown. The $\sqrt{\hat{s}}$ as a function of $\theta_{\ell\ell}$ and $\phi_{\ell\ell}$ given by the ANN is shown in the right panel of Fig. 9. We find that, $\sqrt{\hat{s}}$ is insensitive to $\phi_{\ell\ell}$. For the case of aQGCs, the $W^\pm$ bosons are typically energetic. As a result, the charged leptons are dominantly back-to-back. We find that, at the vicinity of $\theta_{\ell\ell} \approx \pi$, $\sqrt{\hat{s}}$ is almost independent of $\phi_{\ell\ell}$, and is approximately a cosine function of $\theta_{\ell\ell}$.

Based on the observations, we assume the relation between $\sqrt{\hat{s}}$ and the momenta of charged leptons can be fitted by an ansatz in Eq. (5.3). Note that, for fixed $E_{\ell^\pm}$ and $\phi_{\ell^\pm} = 0$, the ansatz has the form $a_1 + a_2\cos(\theta_{\ell^+} - \theta_{\ell^-})$. For fixed $\theta_{\ell^\pm}$ and $\phi_{\ell^\pm} = 0$, the ansatz has the form $b_1 + b_2(E_{\ell^+} + E_{\ell^-}) + b_3 E_{\ell^+} E_{\ell^-}$. Besides, the ansatz is a cosine function

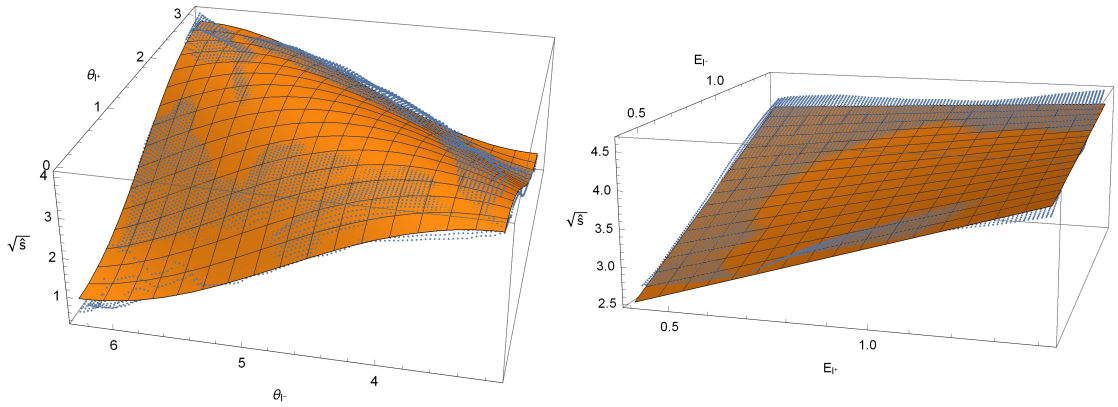


Figure 8: The relationship between $\hat{s}$ and the 4-momenta of charged leptons in Eqs. (5.1) and (5.2) given by the ANN (the dots). The left panel is for Eq. (5.1) and the right panel is for Eq. (5.2). The curved surfaces are functions fitted by using the anstaz $a_1 + a_2 \cos(\theta_{\ell+} - \theta_{\ell-})$ (the left panel) and anstaz $b_1 + b_2(E_{\ell+} + E_{\ell-}) + b_3 E_{\ell+} E_{\ell-}$ (the right panel).

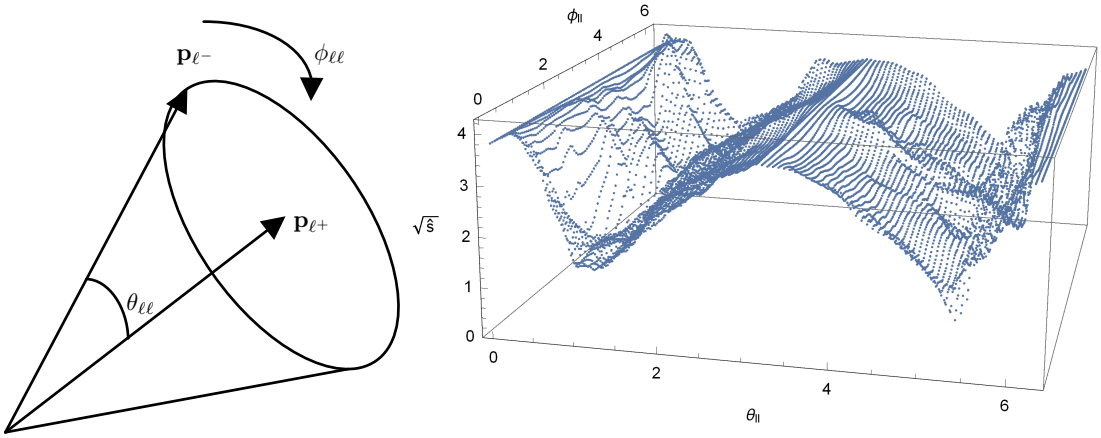


Figure 9: The directions of the momenta of charged leptons used to study the relationship between $\hat{s}$ and the angles between charged leptons are shown in the left panel. The $\hat{s}$ as a function of $\theta_{\ell\ell}$ and $\phi_{\ell\ell}$ given by the ANN is shown in the right panel.

of $\theta_{\ell\ell}$ and is independent of $\phi_{\ell\ell}$.

$$\begin{aligned}
&\sqrt{\hat{s}} \approx c_1 + c_2\,(E_{\ell+} + E_{\ell-}) + (c_3 + c_4\,(E_{\ell+} + E_{\ell-}) + c_5 E_{\ell+} E_{\ell-})\cos(\theta_{\ell\ell}) \\
&c_1 = 1.33642 \text{ TeV}, \quad c_2 = 0.511962, \\
&c_3 = -0.355933 \text{ TeV}, \quad c_4 = -0.778735, \quad c_5 = 0.298186 \text{ TeV}^{-1}
\end{aligned} \tag{5.3}$$

Using the training data-set, the relation between $\sqrt{\hat{s}}$ and the momenta of charged leptons are fitted using the ansatz in Eq. (5.3), the results are also shown in Eq. (5.3).

Denoting $\sqrt{\hat{s}_{\rm lep}}$ as the $\sqrt{\hat{s}}$ predicted by Eq. (5.3), the normalized distribution of $|\sqrt{\hat{s}_{\rm lep}} - \sqrt{\hat{s}_{\rm 2l}}|$ for the V_0 validation data-set is shown in Fig. 10. We find that, Eq. (5.3) can approximate the ANN well. The normalized distributions of $\Delta\sqrt{\hat{s}}$ for $\hat{s}_{\rm ap}$, $\hat{s}_{\rm lep}$ and $\hat{s}_{\rm 2l}$

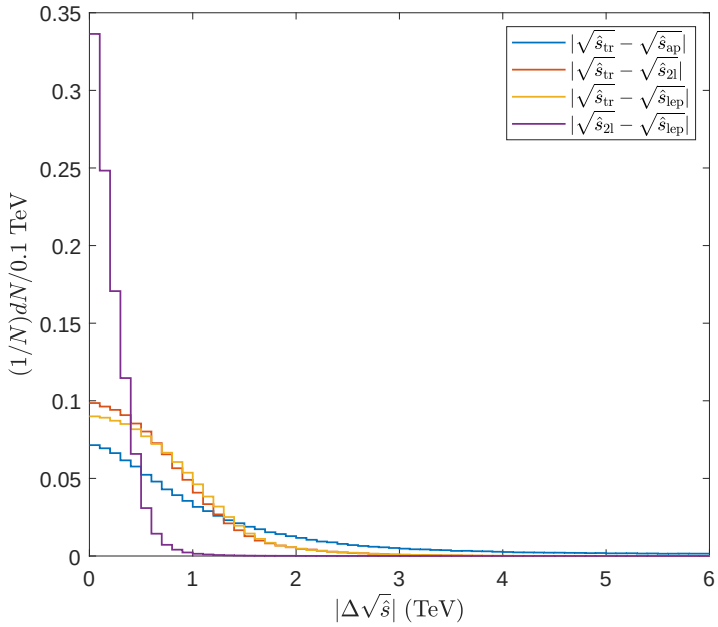


Figure 10: The normalized distributions of $|\sqrt{\hat{s}_{\rm lep}} - \sqrt{\hat{s}_{\rm 2l}}|$, $|\sqrt{\hat{s}_{\rm tr}} - \sqrt{\hat{s}_{\rm lep}}|$, $|\sqrt{\hat{s}_{\rm tr}} - \sqrt{\hat{s}_{\rm 2l}}|$ and $|\sqrt{\hat{s}_{\rm tr}} - \sqrt{\hat{s}_{\rm ap}}|$.

are also shown in Fig. 10. It can be seen that, Eq. (5.3) is able to achieve comparable results to the ANN. Meanwhile, as an approximation found by the ANN, Eq. (5.3) is much better than Eq. (3.2).

The ANN with $n_1 = 8$ contains 9025 trainable parameters. As a contrast, the ansatz in Eq. (5.3) has only five fitting parameters. Besides, Eq. (5.3) is no longer an overly complicated expression which is hard to read. One can already see some patterns from Eq. (5.3). For example, $\hat{s}$ is insensitive to $\phi_{\ell\ell}$, and is approximately a linear function of $E_{\ell^+} + E_{\ell^-}$ when $\cos(\theta_{\ell\ell}) = 0$.

6 Expected constraints on the aQGCs

Where to find the signals of the NP is one of the most important questions in the study of NP. Since the signals of aQGCs are not observed yet, the objective of this section is to investigate the sensitivity of VBS processes to the aQGCs. In this section we study the signals and backgrounds with the help of the ANN. To take into account the unitarity bounds, $\hat{s}$ is necessary. The $\hat{s}$ reconstructed by the ANN approach is made use of to apply the unitarity bounds which are important in the study of an EFT.

6.1 One ANN for all couplings

We have confirmed in Sec. 4 that the ANN does not use the information about which coupling the events come from. For simplicity, and on the other hand, to have more

sufficient training samples, we combine the training data-sets of $V_{0,1,2,3}$ to one data-set, and use this data-set to train one ANN for all couplings.

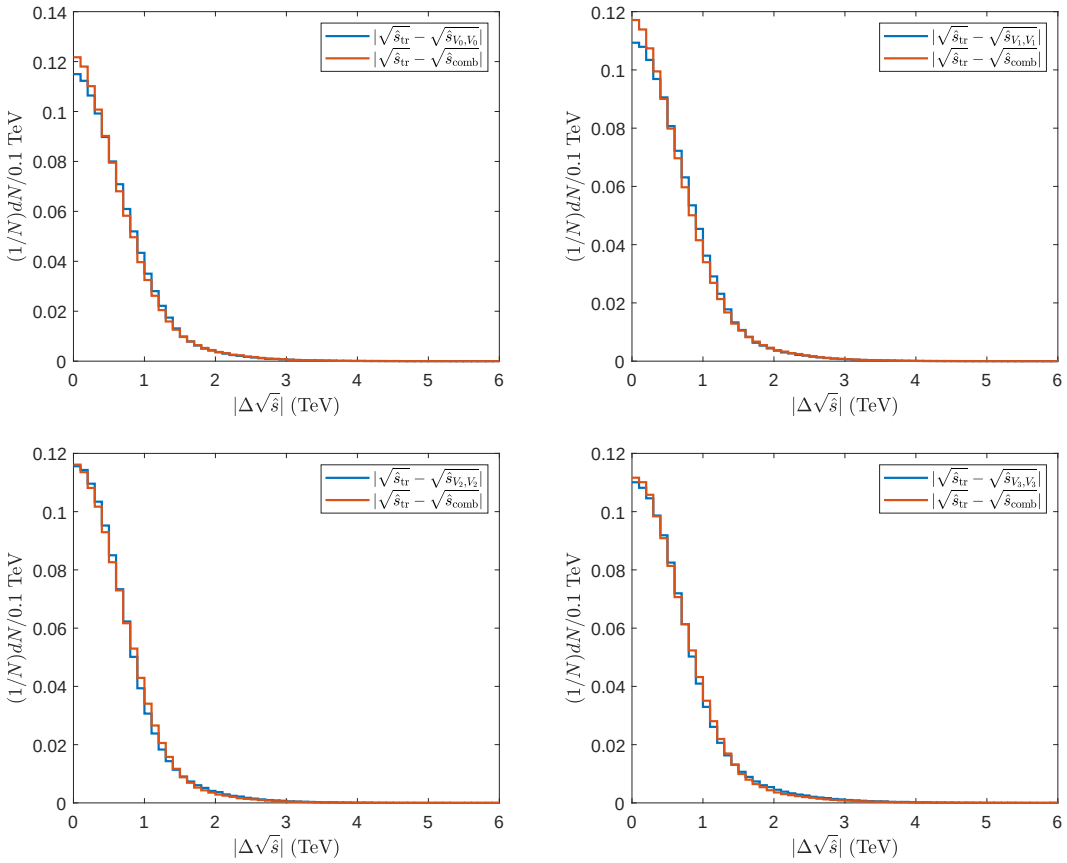


Figure 11: The normalized distributions of $\Delta\sqrt{s}$ for $\hat{s}_{\rm comb}$ compared with those for $\hat{s}_{V_i,V_i}$.

Denoting $\hat{s}_{\rm comb}$ as $\hat{s}$ of the events in validation data-sets predicted by the ANN trained with the combined data-set, normalized distributions of $\Delta\sqrt{\hat{s}}$ for $\hat{s}_{\rm comb}$ and $\hat{s}_{V_i,V_i}$ are compared in Fig. 11. We find that for $V_{0,1}$ vertices, $\hat{s}_{\rm comb}$ are slightly better than $\hat{s}_{V_0,V_0}$ and $\hat{s}_{V_1,V_1}$, for $V_{2,3}$ vertices, $\hat{s}_{\rm comb}$ are about the same as $\hat{s}_{V_2,V_2}$ and $\hat{s}_{V_3,V_3}$. In the remainder of this section, we use $\hat{s}_{\rm comb}$.

6.2 Signals and backgrounds

At the LHC, the $t\bar{t}+Nj$ production contribute to the backgrounds due to the b-jet mistag. The Feynman diagrams in the case of $N = 0$ are shown in Fig. 12. (b). The cross section of inclusive $t\bar{t}$ production is about 888 pb [90], with the 77% [91] b-tagging efficiency, the inclusive $t\bar{t}$ production would lead to a $jj\ell^+\ell^-\nu\bar{\nu}$ background whose cross section is about 2.32 pb. Apart from the $t\bar{t}$ backgrounds, significant irreducible backgrounds can arise from the SM processes which lead to the same final state $\ell^+\ell^-\nu\bar{\nu}jj$. The typical Feynman diagrams at tree level are shown in Fig. 12. (a), which are often categorized as the electroweak VBS (EW-VBS), electroweak non-VBS (EW-non-VBS) and QCD processes. To highlight

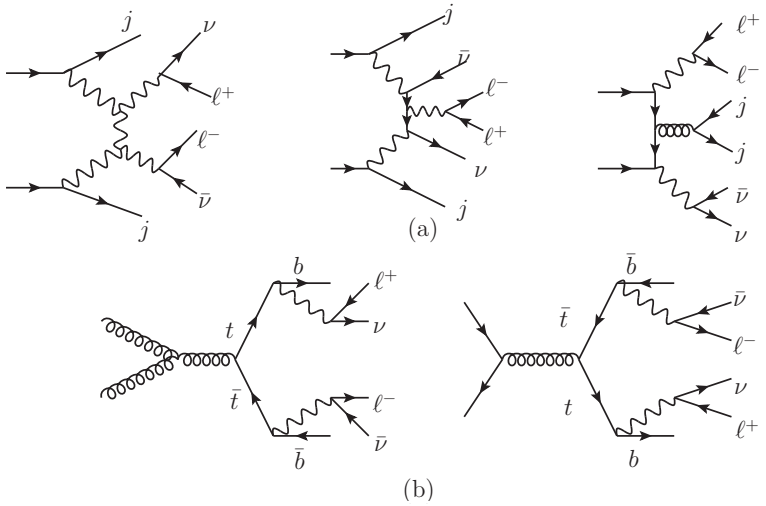


Figure 12: The typical Feynman diagrams of the backgrounds.

the contributions from aQGCs, the contributions from EW-VBS diagrams including those contain the SM $\gamma\gamma W^+W^-$ coupling are also considered as parts of backgrounds. In the following, the backgrounds shown in Fig. 12. (a) are denoted as 'SM', and the backgrounds in Fig. 12. (b) are denoted as '$t\bar{t}$'.

We use the event selection strategy in Ref. [52],

$$\begin{aligned} &M_{jj} > 150 \text{ GeV}, \ \Delta y_{jj} > 1.2, \ \ |\cos(\phi_{LM})| > 0.3, \\ &\cos(\theta_{\ell\ell}) < 0, \ \ \hat{s}_{\text{ap}} > 1.5 \text{ TeV}^2, \ \ M_{o1} > 600 \text{ GeV}, \end{aligned} \tag{6.1}$$

where M_{jj} and Δy_{jj} are invariant mass and difference between the rapidities of the hardest two jets, ϕ_{LM} is the angle between the transverse missing momentum and the sum of transverse momenta of charged leptons, i.e. the angle between $\mathbf{p}_T^{\ell^+} + \mathbf{p}_T^{\ell^-}$ and $\mathbf{p}_T^{\text{miss}}$, $\theta_{\ell\ell}$ is the angle between the charged leptons, and [92]

$$M_{o1} \equiv \sqrt{\left(|\mathbf{p}_T^{\ell^+}| + |\mathbf{p}_T^{\ell^-}| + |\mathbf{p}_{\text{T}}^{\text{miss}}|\right)^2 - \left|\mathbf{p}_T^{\ell^+} + \mathbf{p}_T^{\ell^-} + \mathbf{p}_{\text{T}}^{\text{miss}}\right|^2}, \tag{6.2}$$

which was found to be very efficient to highlight the signals of aQGCs in the study of same sign WW scattering. In this paper, we use $\hat{s}_{\text{comb}}$ instead of $\hat{s}_{\text{ap}}$ and adjust the cut to $\hat{s}_{\text{comb}} > 2.25$ TeV^2. $\hat{s}$ is not well defined in the cases such as the $t\bar{t}$ background events, nevertheless, $\hat{s}_{\text{comb}}$ can still serve as an observable to discriminate the signal events from the backgrounds. The normalized distributions of $\sqrt{\hat{s}_{\text{comb}}}$ are shown in Fig. 13. It can be seen that, for a background event, $\hat{s}_{\text{comb}}$ is generally smaller than 2.25 TeV^2, which is not the case for a signal event.

By using the event selection strategy in Eq. (6.1), the cut flow is shown in Table 2. From Table 2, it can be seen that the cuts can reduce the backgrounds significantly while preserving much of the signals events. For the $pp \to t\bar{t} + Nj$ backgrounds, the cut efficiency for $N = 0$ is the lowest mainly because the $N_j \leq 5$ cut can increase the cut efficiencies for the cases of $N > 0$. An upper bound of the $pp \to t\bar{t} + Nj$ backgrounds is estimated by

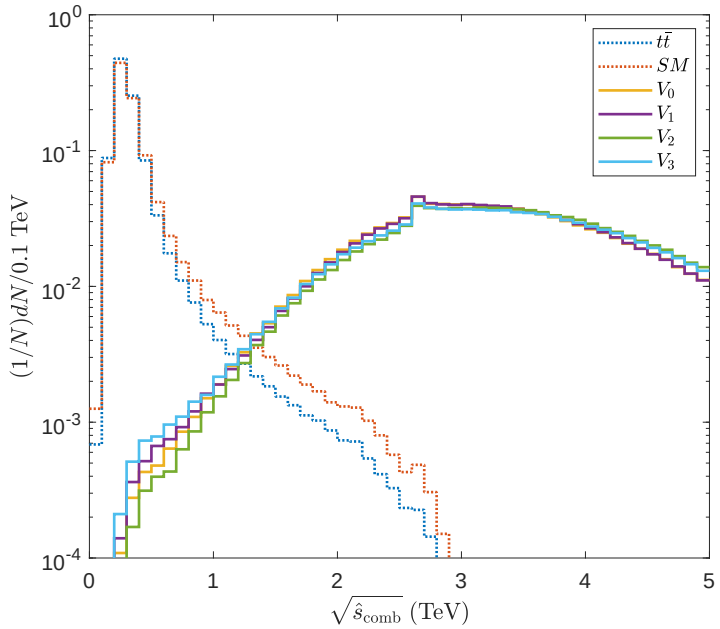


Figure 13: The normalized distributions of $\sqrt{\hat{s}_{\rm comb}}$ for the signal events and background events.

σ(fb)	$\alpha_0 = 0.013$ (TeV^{-2})	$\alpha_1 = 0.021$ (TeV^{-2})	$\alpha_2 = 0.38$ (TeV^{-4})	$\alpha_3 = 0.69$ (TeV^{-4})	SM	$t\bar{t}$
before cuts	1.66	0.29	0.49	0.12	724.16	24938.24
$N_\ell = 2$ $5 \geq N_j \geq 2$	0.91	0.16	0.26	0.064	308.63	8162.41
$M_{jj} > 150$ GeV $\Delta y_{jj} > 1.2$	0.76	0.13	0.22	0.053	111.44	2766.76
$\lvert\cos(\phi_{Lm})\rvert > 0.3$	0.69	0.12	0.21	0.050	91.13	2233.19
$\cos(\theta_{\ell\ell}) < 0$	0.69	0.12	0.20	0.049	49.09	1301.81
$M_{o1} > 600$ GeV	0.64	0.11	0.20	0.046	0.61	2.34
$\hat{s}_{\rm comb} > 2.25$ TeV^2	0.64	0.11	0.19	0.046	0.38	1.60

Table 2: The effect of the cuts on the process $pp \to \ell^+\ell^-\nu\bar{\nu}jj$. The cross sections of signal and background events are given in fb. The result of $t\bar{t} + Nj$ with $N = 0$ is shown as an example, the effect of b-tagging is not included in this table which will reduce the cross-section from 24938.24 fb to 1319.23 fb with 77% b-tagging efficiency.

using the efficiency of $N = 0$ for all values of N. Then, the $pp \to t\bar{t} + Nj$ backgrounds is reduced from 2.32 (pb) to about 0.15 (fb).

Amplitudes	α_0	α_1	α_2	α_3	α_4
$\mathcal{M}_{++++}$	$\mathcal{O}(\hat{s})$	$\mathcal{O}(\hat{s})$	$2\alpha_2\hat{s}^2$	$\frac{1}{2}\alpha_3\hat{s}^2$	$\mathcal{O}(\hat{s}^0)$
$\mathcal{M}_{++--}$	$\mathcal{O}(\hat{s})$	$\mathcal{O}(\hat{s})$	$2\alpha_2\hat{s}^2$	$\frac{1}{2}\alpha_3\hat{s}^2$	$\frac{1}{4}\alpha_4\hat{s}^2\,(\cos(2\theta)+3)$
$\mathcal{M}_{++00}$	$\alpha_0\frac{\hat{s}^2}{M_W^2}$	$\frac{1}{4}\alpha_1\frac{\hat{s}^2}{M_W^2}$	$\mathcal{O}(\hat{s})$	$\mathcal{O}(\hat{s})$	$\mathcal{O}(\hat{s})$
$\mathcal{M}_{+-+-}$	$\mathcal{O}(\hat{s}^0)$	$\mathcal{O}(\hat{s})$	$\mathcal{O}(\hat{s}^0)$	$\frac{1}{2}e^{2i\phi}\alpha_3\hat{s}^2\cos^4(\frac{\theta}{2})$	$\alpha_4 e^{2i\phi}s^2\cos^4(\frac{\theta}{2})$
$\mathcal{M}_{+--+}$	$\mathcal{O}(\hat{s}^0)$	$\mathcal{O}(\hat{s})$	$\mathcal{O}(\hat{s}^0)$	$\frac{1}{2}e^{-2i\phi}\alpha_3\hat{s}^2\sin^4(\frac{\theta}{2})$	$\alpha_4 e^{-2i\phi}\hat{s}^2\sin^4(\frac{\theta}{2})$
$\mathcal{M}_{+-00}$	$\mathcal{O}(\hat{s}^0)$	$\frac{e^{2i\phi}\alpha_1\hat{s}^2\sin^2(\theta)}{8M_W^2}$	$\mathcal{O}(\hat{s}^0)$	$\mathcal{O}(\hat{s})$	$\mathcal{O}(\hat{s})$

Table 3: The helicity amplitudes at the order of $\mathcal{O}(s^2)$.

6.3 Unitarity bounds

As an EFT, the SMEFT is only valid under a certain energy scale. The cross-section of the VBS process with contributions from aQGCs included grows significantly at high energies. On one hand, at higher energies the VBS process is ideal to search for aQGCs. On the other hand, the cross-section will violate unitarity at a certain high energy, which provides a signature indicating that the SMEFT is not valid. The violation of unitarity can be avoided by unitarization methods such as K-matrix unitarization [80], T-matrix unitarization [93], form factor method [79, 80], as well as dispersion relation method [94, 95]. It has been pointed out that, the constraints on the coefficients dependent on the method used [96], and it has been emphasised that unitrization defeats the model-independent purpose of using an EFT [63]. Therefore, we present our results using a procedure independent of unitarization methods.

Considering the subprocess $\gamma_{\lambda_1}\gamma_{\lambda_2} \to W^-_{\lambda_3}W^+_{\lambda_4}$, where $\lambda_{1,2} = \pm 1$ and $\lambda_{3,4} = \pm 1, 0$ correspond to the helicities of the vector bosons, in the c.m. frame of two photons with **z**-axis along the flight direction of γ_{λ_1}, the amplitudes can be expanded as [97]

$$\mathcal{M}(\gamma_{\lambda_1}\gamma_{\lambda_2} \to W^-_{\lambda_3}W^+_{\lambda_4}) = 8\pi\sum_J (2J+1)\sqrt{1+\delta_{\lambda_1\lambda_2}}e^{i(\lambda-\lambda')\phi}d^J_{\lambda\lambda'}(\theta)T^J \tag{6.3}$$

where θ and ϕ are zenith and azimuth angles of the W^- boson, $\lambda = \lambda_1 - \lambda_2$, $\lambda' = \lambda_3 - \lambda_4$ and $d^J_{\lambda\lambda'}(\theta)$ are the Wigner D-functions [97]. The partial wave unitarity bound is $|T^J| \leq 2$ [9].

For the $\gamma\gamma \to W^+W^-$, 36 different helicity amplitudes can be obtained. The number of amplitudes can be reduced by using $\mathcal{M}_{\lambda_1,\lambda_2,\lambda_3,\lambda_4}(\theta) = (-1)^{\lambda_1-\lambda_2-\lambda_3+\lambda_4}\mathcal{M}_{-\lambda_1,-\lambda_2,-\lambda_3,-\lambda_4}(\theta)$. It is only necessary to keep the terms at the leading order ($\mathcal{O}(\hat{s}^2)$). The helicity amplitudes at the leading order are list in Table. 3. The tightest bounds are

$$\hat{s}^2 \leq \frac{16\sqrt{2}\pi M_W^2}{|\alpha_0|},\quad \hat{s}^2 \leq \frac{64\sqrt{2}\pi M_W^2}{|\alpha_1|},\quad \hat{s}^2 \leq \frac{8\sqrt{2}\pi}{|\alpha_2|},\quad \hat{s}^2 \leq \frac{32\sqrt{2}\pi}{|\alpha_3|},\quad \hat{s}^2 \leq \frac{24\sqrt{2}\pi}{|\alpha_4|}. \tag{6.4}$$

The partial wave unitarity bound has been widely used in previous studies [59, 60, 98–103]. To avoid the violation of unitarity, the partial wave unitarity bound was often used as constraints on the coefficients of the high dimensional operators. Note that, in Eq. (6.4), the unitarity bounds are presented as constraints on $\hat{s}$ instead of the coefficients. Due to

the PDF, the $\hat{s}$ of the subprocess is not a fixed value, which brings difficulties in setting constraints on the coefficients directly. Therefore, in this paper we use a matching procedure [104, 105] instead. The matching procedure is built based on the idea that, to take validity into account, the constraints obtained by experiments should be reported as functions of energy scales [5], and has been introduced in the studies of the aQGCs [11, 51]. Such a matching procedure is independent of unitarization methods and can be applied in experiments. The matching procedure in this paper is also very similar to the 'clipping' method which also cuts off the signal events violating unitarity according to $\hat{s}$ [76, 106], except that we also cut off the backgrounds so one can compare the signals with backgrounds under a same $\hat{s}$ cut.

We use Eq. (6.4) as a cut on $\hat{s}$, and compare the cross-sections with and without aQGCs under a same energy cut. We shall emphasis that, although this approach is called 'unitarity bound', using this approach we are actually not applying any constraints or unitarizations. In any case, it is practicable to compare NP and the SM under a certain energy scale. Especially, it is necessary in the detailed study of the Wilson coefficients in an EFT because the Wilson coefficients are functions of the energy scale. This matching procedure is independent of whether or not the unitarity bounds are imposed. We merely choose a matching energy scale such that the unitarity is guaranteed. Specifically, we choose the energy scale as the maximally allowed energy scale according to the coefficients of the aQGCs in the sense of unitarity.

σ(fb)	$\alpha_0 = 0.013$ (TeV^{-2})	$\alpha_1 = 0.021$ (TeV^{-2})	$\alpha_2 = 0.38$ (TeV^{-4})	$\alpha_3 = 0.69$ (TeV^{-4})
$\sqrt{\hat{s}}_{\max}$ (TeV)	2.44	3.06	3.11	2.79
before unitarity bounds (fb)	0.64	0.11	0.19	0.046
after unitarity bounds (fb)	0.083	0.042	0.068	0.028

Table 4: The $\sqrt{\hat{s}}_{\max}$ correspond to the largest coefficients in the ranges listed in Table 1, and the cross-sections before and after the energy cuts in Eq. (6.4).

For the largest coefficients listed in Table 1, the maximally allowed energy scales (denoted as $\sqrt{\hat{s}}_{\max}$) according to Eq. (6.4) are listed in Table 4. The effect of the unitarity bounds are also shown in Table 4. It can be seen that, the unitarity bounds have great suppressive effects on the cross-sections. Especially for V_0, the cross-section is reduced by about an order of magnitude. Such a significant suppression indicates the necessity of the unitarity bounds.

6.4 Signal significance

The sensitivity of the process $pp \to jj\ell^+\ell^-\nu\bar{\nu}$ to the aQGCs can be estimated with the help of statistical significance defined as $\mathcal{S}_{stat} \equiv N_S/\sqrt{N_S + N_B}$, where N_S is the number of signal events, and N_B is the number of the background events. It has been shown that, within the current ranges of coefficients of the aQGCs, the interference terms can also be

neglected [52]. For simplicity, the cross-sections are calculated with the above contributions neglected.

We scan the parameter spaces larger than the constraints listed in Table 1 because the unitarity bounds have significant suppressive effects. The unitarity bounds are applied for each coefficient individually, and are applied according to Eq. (6.4). The cross-sections for aQGCs, the SM and $t\bar{t}$ backgrounds are denoted as σ_{V_i}, σ_{SM} and $\sigma_{t\bar{t}+Nj}$, respectively. After the cuts listed in Table 2 and after the unitarity bounds, the cross-sections as functions of the coefficients are shown in Fig. 14. Note that, although the cross-sections of the backgrounds are not functions of the coefficients of aQGCs, we compare the cross-sections of the backgrounds under different energy scales which are related with the coefficients of aQGCs, consequently, the cross-sections of the backgrounds appear to become functions of the coefficients of aQGCs. Without the unitarity bounds, the cross-sections of the signals should be quadratic functions of the coefficients. As we can see from Fig. 14, this is greatly changed by the unitarity bounds.

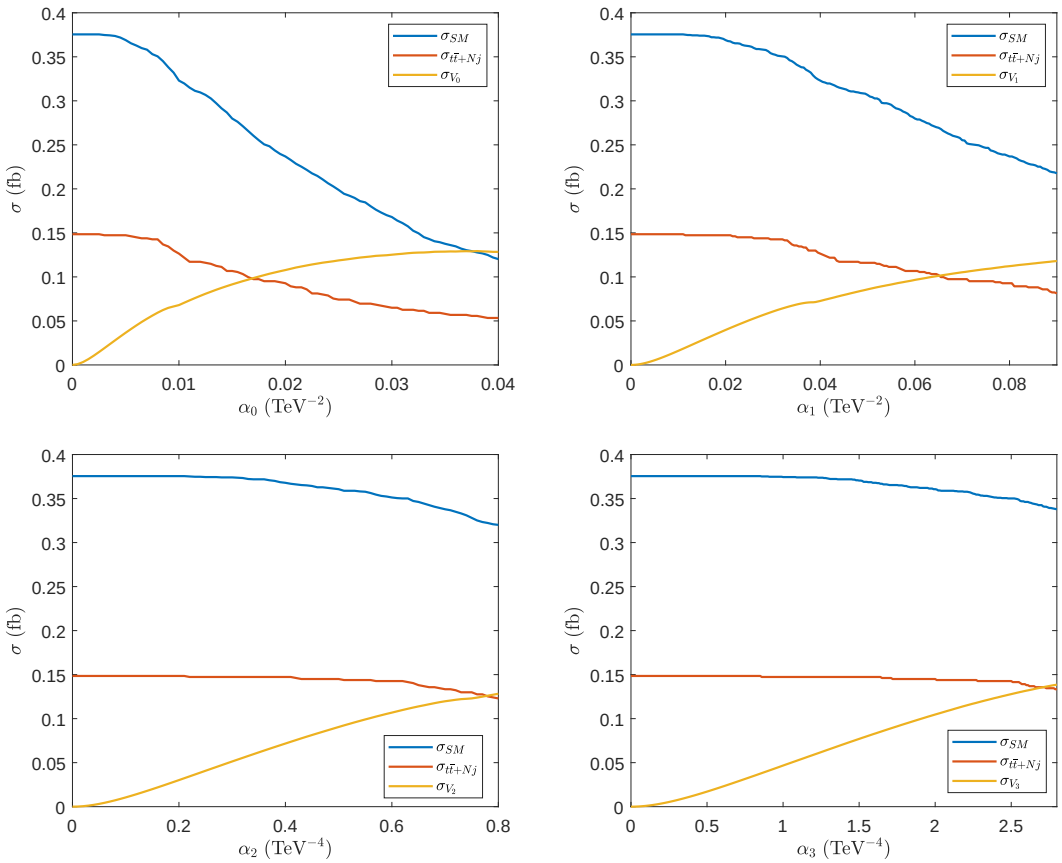


Figure 14: The cross-sections as functions of the coefficients of aQGCs after the cuts listed in Table 2 and after the unitarity bounds.

$\mathcal{S}_{stat}$ for aQGCs are calculated and shown in Fig. 15. $\mathcal{S}_{stat}$ in Fig. 15 is calculated at luminosity $\mathcal{L} = 139$ fb^{-1} which is the total luminosity at 13 TeV LHC [107, 108]. It can

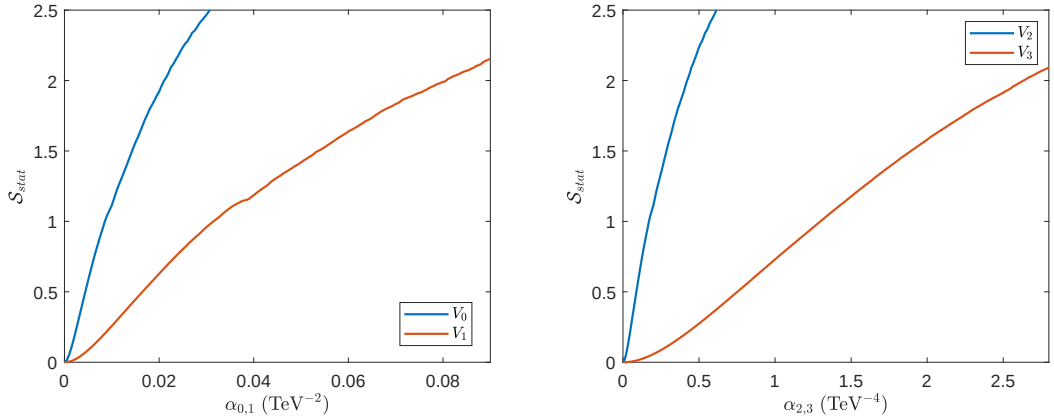


Figure 15: The signal significances at $\mathcal{L} = 139$ fb^{-1} as functions of the coefficients of aQGCs.

	139 fb^{-1}	300 fb^{-1}
$\lvert\alpha_0\rvert$ (TeV^{-2})	< 0.021	< 0.013
$\lvert\alpha_1\rvert$ (TeV^{-2})	< 0.081	< 0.048
$\lvert\alpha_2\rvert$ (TeV^{-4})	< 0.42	< 0.26
$\lvert\alpha_3\rvert$ (TeV^{-4})	< 2.63	< 1.72

Table 5: The expected constraints on the coefficients of the anomalous $\gamma\gamma WW$ couplings at 13 TeV with $\mathcal{L} = 139$ fb^{-1} and $\mathcal{L} = 300$ fb^{-1} when $\mathcal{S}_{stat} < 2$.

be found in Fig. 15 that the process $pp \to jj\ell^+\ell^-\nu\bar{\nu}$ is sensitive to the $V_{0,2}$ vertices. The expected constraints are calculated assuming the signals of aQGCs are not observed with $\mathcal{S}_{stat} \geq 2$, which are shown in Table 5. The results for possible future LHC luminosity $\mathcal{L} = 300$ fb^{-1} [109] are also shown in Table 5. A comparison of Tables 1 and 5 shows that, except for V_2, the constraints at $\mathcal{L} = 139$ fb^{-1} in Table 5 is a bit less stringent, while the constraints in Table 1 is given at $\mathcal{L} = 35.9$ fb^{-1} by studying the production of $W\gamma$. The main reason is that results in Table 1 do not take into account unitarity bounds. The fact that constraints with unitarity bounds considered are significantly less stringent were also observed in the studies using 'clipping' method [76]. From the results in Figs. 14, 15 and Table 5, one can see that when the unitarity bounds are applied, it is very important to increase the luminosity in order to narrow down the coefficient spaces. This is the problem of the narrow 'EFT triangles' which has been pointed out in previous studies [13, 92, 110], and it has been suggested that multi-operator analysis and combination of different processes are also important. We shall emphasis that, the above arguments are based on the pessimistic assumption that NP signals will not be discovered. This in turn just shows the importance of the high-energy region, where plenty room has been left for the discovery of new resonances.

7 Summary

In the study of the SMEFT, the energy scale of a process is an important parameter. However, reconstruction of the energy scales for processes at the LHC is difficult when there are two neutrinos in final states. The energy scale of the sub-process $\gamma\gamma \to W^+W^-$ in the VBS process $pp \to jj\ell^+\ell^-\nu\bar{\nu}$ is such a case. In this paper, we study the contribution of aQGCs in the process $pp \to jj\ell^+\ell^-\nu\bar{\nu}$ with the focus on the energy scale of the sub-process $\gamma\gamma \to W^+W^-$. The method we are using is the ANN.

We show that ANN, as a technique that has proven itself in several areas of HEP, is powerful when studying $\hat{s}$ of the process $pp \to jj\ell^+\ell^-\nu\bar{\nu}$. The results of the ANNs are much better than the approximation derived from kinematic analysis. With the help of ANNs, we investigate the information about $\hat{s}$ hidden in the final state. It can be shown that, the importance of different sectors can be ordered as $p^{\ell^\pm} > \mathbf{p}_T^{\text{miss}} > p^{\text{jet}}$. Apart from that, which coupling is being studied, and the collision energy are two pieces of information that are hardly used.

With the help of the ANN approach, we find another approximate formula for $\hat{s}$ which is a function of three variables $\theta_{\ell\ell}$, E_{ℓ^+} and E_{ℓ^-} and contains only five fitting parameters, as presented in Eq. (5.3). Eq. (5.3) has comparable accuracy as the ANN trained with 4-momenta of charged leptons which has 9075 fitting parameters, and is more understandable than the ANN. In addition, Eq. (5.3) is much better than the approximation derived from kinematic analysis.

The unitarity bounds and the signal significances of aQGCs are also studied in this paper. It can be shown that, $\hat{s}$ reconstructed by the ANN approach serves as an observable powerful in discriminating the signal events from the backgrounds. With $\hat{s}$, the unitarity bounds can be applied. The unitarity bounds have significant suppressive effects, and therefore are necessary. With unitarity bounds applied, the cross-sections and the signal significances of aQGCs are studied. The expected constraints at $\mathcal{L} = 139$ and 300 fb^{-1} are obtained. The constraints from the process $pp \to jj\ell^+\ell^-\nu\bar{\nu}$ can contribute to the combined limits.

ACKNOWLEDGMENT

This work is supported in part by the National Natural Science Foundation of China under Grants No.11905093 and No.12047570, the Natural Science Foundation of the Liaoning Scientific Committee (No.2019-BS-154) and the Outstanding Research Cultivation Program of Liaoning Normal University (No.21GDL004).

References

[1] S. Weinberg, *Baryon and Lepton Nonconserving Processes*, *Phys. Rev. Lett.* **43** (1979) 1566.

[2] B. Grzadkowski, M. Iskrzynski, M. Misiak and J. Rosiek, *Dimension-Six Terms in the Standard Model Lagrangian*, *JHEP* **10** (2010) 085 [1008.4884].

[3] S. Willenbrock and C. Zhang, *Effective Field Theory Beyond the Standard Model*, *Ann. Rev. Nucl. Part. Sci.* **64** (2014) 83 [1401.0470].

[4] E. Masso, *An Effective Guide to Beyond the Standard Model Physics*, *JHEP* **10** (2014) 128 [1406.6376].

[5] R. Contino, A. Falkowski, F. Goertz, C. Grojean and F. Riva, *On the Validity of the Effective Field Theory Approach to SM Precision Tests*, *JHEP* **07** (2016) 144 [1604.06444].

[6] T. Lee and C.-N. Yang, *THEORETICAL DISCUSSIONS ON POSSIBLE HIGH-ENERGY NEUTRINO EXPERIMENTS*, *Phys. Rev. Lett.* **4** (1960) 307.

[7] M. Froissart, *Asymptotic behavior and subtractions in the Mandelstam representation*, *Phys. Rev.* **123** (1961) 1053.

[8] G. Passarino, *W W scattering and perturbative unitarity*, *Nucl. Phys. B* **343** (1990) 31.

[9] T. Corbett, O. J. P. Éboli and M. C. Gonzalez-Garcia, *Unitarity Constraints on Dimension-Six Operators*, *Phys. Rev. D* **91** (2015) 035014 [1411.5026].

[10] A. Alboteanu, W. Kilian and J. Reuter, *Resonances and Unitarity in Weak Boson Scattering at the LHC*, *JHEP* **11** (2008) 010 [0806.4145].

[11] Y.-C. Guo, Y.-Y. Wang, J.-C. Yang and C.-X. Yue, *Constraints on anomalous quartic gauge couplings via $W\gamma jj$ production at the LHC*, *Chin. Phys. C* **44** (2020) 123105 [2002.03326].

[12] A. Falkowski, M. Gonzalez-Alonso, A. Greljo, D. Marzocca and M. Son, *Anomalous Triple Gauge Couplings in the Effective Field Theory Approach at the LHC*, *JHEP* **02** (2017) 115 [1609.06312].

[13] G. Chaudhary, J. Kalinowski, M. Kaur, P. Kozów, K. Sandeep, M. Szleper et al., *EFT triangles in the same-sign WW scattering process at the HL-LHC and HE-LHC*, *Eur. Phys. J. C* **80** (2020) 181 [1906.10769].

[14] A. Ballestrero, E. Maina and G. Pelliccioli, *W boson polarization in vector boson scattering at the LHC*, *JHEP* **03** (2018) 170 [1710.09339].

[15] CMS collaboration, *Measurement of the Polarization of W Bosons with Large Transverse Momenta in W+Jets Events at the LHC*, *Phys. Rev. Lett.* **107** (2011) 021802 [1104.3829].

[16] ATLAS collaboration, *Measurement of the polarisation of W bosons produced with large transverse momentum in pp collisions at $\sqrt{s} = 7$ TeV with the ATLAS experiment*, *Eur. Phys. J. C* **72** (2012) 2001 [1203.2165].

[17] K. Doroba, J. Kalinowski, J. Kuczmarski, S. Pokorski, J. Rosiek, M. Szleper et al., *The $W_L W_L$ Scattering at the LHC: Improving the Selection Criteria*, *Phys. Rev. D* **86** (2012) 036011 [1201.2768].

[18] ATLAS collaboration, *Measurement of the W boson polarisation in $t\bar{t}$ events from pp collisions at $\sqrt{s} = 8$ TeV in the lepton + jets channel with ATLAS*, *Eur. Phys. J. C* **77** (2017) 264 [1612.02577].

[19] CMS collaboration, *Measurement of the W boson helicity fractions in the decays of top quark pairs to lepton + jets final states produced in pp collisions at $\sqrt{s} = 8$TeV*, *Phys. Lett. B* **762** (2016) 512 [1605.09047].

[20] M. Peruzzi, *First measurement of vector boson polarization at LHC*, Ph.D. thesis, Zurich, ETH, 2011.

[21] J. Searcy, L. Huang, M.-A. Pleier and J. Zhu, *Determination of the WW polarization fractions in $pp \to W^{\pm}W^{\pm}jj$ using a deep machine learning technique*, *Phys. Rev. D* **93** (2016) 094033 [1510.01691].

[22] J. Lee, N. Chanon, A. Levin, J. Li, M. Lu, Q. Li et al., *Polarization fraction measurement in same-sign WW scattering using deep learning*, *Phys. Rev. D* **99** (2019) 033004 [1812.07591].

[23] J. Lee, N. Chanon, A. Levin, J. Li, M. Lu, Q. Li et al., *Polarization fraction measurement in ZZ scattering using deep learning*, *Phys. Rev. D* **100** (2019) 116010 [1908.05196].

[24] K. Lasocha, E. Richter-Was, D. Tracz, Z. Was and P. Winkowska, *Machine learning classification: Case of Higgs boson CP state in $H \to \tau\tau$ decay at the LHC*, *Phys. Rev. D* **100** (2019) 113001 [1812.08140].

[25] L. Lonnblad, C. Peterson and T. Rognvaldsson, *Using neural networks to identify jets*, *Nucl. Phys. B* **349** (1991) 675.

[26] V. Innocente, Y. F. Wang and Z. P. Zhang, *Identification of tau decays using a neural network*, *Nucl. Instrum. Meth. A* **323** (1992) 647.

[27] B. Holdom and Q.-S. Yan, *Searches for the t' of a fourth family*, *Phys. Rev. D* **83** (2011) 114031 [1101.3844].

[28] A. Radovic, M. Williams, D. Rousseau, M. Kagan, D. Bonacorsi, A. Himmel et al., *Machine learning at the energy and intensity frontiers of particle physics*, *Nature* **560** (2018) 41.

[29] P. Baldi, P. Sadowski and D. Whiteson, *Searching for Exotic Particles in High-Energy Physics with Deep Learning*, *Nature Commun.* **5** (2014) 4308 [1402.4735].

[30] J. Ren, L. Wu, J. M. Yang and J. Zhao, *Exploring supersymmetry with machine learning*, *Nucl. Phys. B* **943** (2019) 114613 [1708.06615].

[31] M. Abdughani, J. Ren, L. Wu and J. M. Yang, *Probing stop pair production at the LHC with graph neural networks*, *JHEP* **08** (2019) 055 [1807.09088].

[32] R. Iten, T. Metger, H. Wilming, L. del Rio and R. Renner, *Discovering physical concepts with neural networks*, *Phys. Rev. Lett.* **124** (2020) 010508.

[33] J. Ren, L. Wu and J. M. Yang, *Unveiling CP property of top-Higgs coupling with graph neural networks at the LHC*, *Phys. Lett. B* **802** (2020) 135198 [1901.05627].

[34] Y.-C. Guo, L. Jiang and J.-C. Yang, *Detecting anomalous quartic gauge couplings using the isolation forest machine learning algorithm*, *Phys. Rev. D* **104** (2021) 035021 [2103.03151].

[35] O. Eboli, M. Gonzalez-Garcia and J. Mizukoshi, *p p —> j j e+- mu+- nu nu and j j e+- mu-+ nu nu at O(alpha(em)**6) and O(alpha(em)**4 alpha(s)**2) for the study of the quartic electroweak gauge boson vertex at CERN LHC*, *Phys. Rev. D* **74** (2006) 073005 [hep-ph/0606118].

[36] O. J. P. Éboli and M. C. Gonzalez-Garcia, *Classifying the bosonic quartic couplings*, *Phys. Rev. D* **93** (2016) 093013 [1604.03555].

[37] M. Born and L. Infeld, *Foundations of the new field theory*, *Proc. Roy. Soc. Lond. A* **144** (1934) 425.

[38] J. Ellis and S.-F. Ge, *Constraining Gluonic Quartic Gauge Coupling Operators with $gg \to \gamma\gamma$* , *Phys. Rev. Lett.* **121** (2018) 041801 [1802.02416].

[39] D. Espriu and F. Mescia, *Unitarity and causality constraints in composite Higgs models*, *Phys. Rev. D* **90** (2014) 015035 [1403.7386].

[40] R. Delgado, A. Dobado, M. Herrero and J. Sanz-Cillero, *One-loop $\gamma\gamma \to W_L^+ W_L^-$ and $\gamma\gamma \to Z_L Z_L$ from the Electroweak Chiral Lagrangian with a light Higgs-like scalar*, *JHEP* **07** (2014) 149 [1404.2866].

[41] S. Fichet and G. von Gersdorff, *Anomalous gauge couplings from composite Higgs and warped extra dimensions*, *JHEP* **03** (2014) 102 [1311.6815].

[42] T. Lee, *A Theory of Spontaneous T Violation*, *Phys. Rev. D* **8** (1973) 1226.

[43] J.-C. Yang and M.-Z. Yang, *Effect of the Charged Higgs Bosons in the Radiative Leptonic Decays of B^- and D^- Mesons*, *Mod. Phys. Lett. A* **31** (2016) 1650012 [1508.00314].

[44] X.-G. He, G. C. Joshi, H. Lew and R. Volkas, *Simplest Z-prime model*, *Phys. Rev. D* **44** (1991) 2118.

[45] J.-X. Hou and C.-X. Yue, *The signatures of the new particles h_2 and $Z_{\mu\tau}$ at e-p colliders in the $U(1)_{L_\mu - L_\tau}$ model*, *Eur. Phys. J. C* **79** (2019) 983 [1905.00627].

[46] K. Mimasu and V. Sanz, *ALPs at Colliders*, *JHEP* **06** (2015) 173 [1409.4792].

[47] C.-X. Yue, M.-Z. Liu and Y.-C. Guo, *Searching for axionlike particles at future ep colliders*, *Phys. Rev. D* **100** (2019) 015020 [1904.10657].

[48] C. Zhang and S.-Y. Zhou, *Positivity bounds on vector boson scattering at the LHC*, *Phys. Rev. D* **100** (2019) 095003 [1808.00010].

[49] Q. Bi, C. Zhang and S.-Y. Zhou, *Positivity constraints on aQGC: carving out the physical parameter space*, *JHEP* **06** (2019) 137 [1902.08977].

[50] C. Anders et al., *Vector boson scattering: Recent experimental and theory developments*, *Rev. Phys.* **3** (2018) 44 [1801.04203].

[51] J.-C. Yang, Y.-C. Guo, C.-X. Yue and Q. Fu, *Constraints on anomalous quartic gauge couplings via $Z\gamma jj$ production at the LHC*, *Phys. Rev. D* **104** (2021) 035015 [2107.01123].

[52] Y.-C. Guo, Y.-Y. Wang and J.-C. Yang, *Constraints on anomalous quartic gauge couplings by $\gamma\gamma \to W^+W^-$ scattering*, *Nucl. Phys. B* **961** (2020) 115222 [1912.10686].

[53] S. Tizchang and S. M. Etesami, *Pinning down the gauge boson couplings in $WW\gamma$ production using forward proton tagging*, *JHEP* **07** (2020) 191 [2004.12203].

[54] C. Zhang and S.-Y. Zhou, *Convex Geometry Perspective to the (Standard Model) Effective Field Theory Space*, *Phys. Rev. Lett.* **125** (2020) 201601 [2005.03047].

[55] C. Degrande, *A basis of dimension-eight operators for anomalous neutral triple gauge boson interactions*, *JHEP* **02** (2014) 101 [1308.6323].

[56] J. Ellis, S.-F. Ge, H.-J. He and R.-Q. Xiao, *Probing the scale of new physics in the $ZZ\gamma$ coupling at e^+e^- colliders*, *Chin. Phys. C* **44** (2020) 063106 [1902.06631].

[57] J. Ellis, H.-J. He and R.-Q. Xiao, *Probing new physics in dimension-8 neutral gauge couplings at e^+e^- colliders*, *Sci. China Phys. Mech. Astron.* **64** (2021) 221062 [2008.04298].

[58] A. Senol, H. Denizli, A. Yilmaz, I. Turk Cakir, K. Y. Oyulmaz, O. Karadeniz et al., *Probing the Effects of Dimension-eight Operators Describing Anomalous Neutral Triple Gauge Boson Interactions at FCC-hh*, *Nucl. Phys. B* **935** (2018) 365 [1805.03475].

[59] Q. Fu, Y.-C. Guo and J.-C. Yang, *The study of unitarity bounds on the neutral triple gauge couplings in the process $e^+e^- \to \ell^+\ell^-\gamma$*, 2102.03623.

[60] G. Perez, M. Sekulla and D. Zeppenfeld, *Anomalous quartic gauge couplings and unitarization for the vector boson scattering process* $pp \to W^+W^+jjX \to \ell^+\nu_\ell\ell^+\nu_\ell jjX$, *Eur. Phys. J. C* **78** (2018) 759 [1807.02707].

[61] C. Arzt, M. Einhorn and J. Wudka, *Patterns of deviation from the standard model*, *Nucl. Phys. B* **433** (1995) 41 [hep-ph/9405214].

[62] B. Henning, X. Lu, T. Melia and H. Murayama, *2, 84, 30, 993, 560, 15456, 11962, 261485, ...: Higher dimension operators in the SM EFT*, *JHEP* **08** (2017) 016 [1512.03433].

[63] D. R. Green, P. Meade and M.-A. Pleier, *Multiboson interactions at the LHC*, *Rev. Mod. Phys.* **89** (2017) 035008 [1610.07572].

[64] ATLAS collaboration, *Evidence for Electroweak Production of* $W^\pm W^\pm jj$ *in pp Collisions at* $\sqrt{s} = 8$ *TeV with the ATLAS Detector*, *Phys. Rev. Lett.* **113** (2014) 141803 [1405.6241].

[65] ATLAS collaboration, *Studies of* $Z\gamma$ *production in association with a high-mass dijet system in pp collisions at* $\sqrt{s} = 8$ *TeV with the ATLAS detector*, *JHEP* **07** (2017) 107 [1705.01966].

[66] CMS collaboration, *Measurement of the cross section for electroweak production of* $Z\gamma$ *in association with two jets and constraints on anomalous quartic gauge couplings in proton–proton collisions at* $\sqrt{s} = 8$ *TeV*, *Phys. Lett. B* **770** (2017) 380 [1702.03025].

[67] CMS collaboration, *Measurement of the cross section for electroweak production of a Z boson, a photon and two jets in proton-proton collisions at* $\sqrt{s} = 13$ *TeV and constraints on anomalous quartic couplings*, *JHEP* **06** (2020) 076 [2002.09902].

[68] CMS collaboration, *Measurement of electroweak-induced production of* $W\gamma$ *with two jets in pp collisions at* $\sqrt{s} = 8$ *TeV and constraints on anomalous quartic gauge couplings*, *JHEP* **06** (2017) 106 [1612.09256].

[69] CMS collaboration, *Measurement of vector boson scattering and constraints on anomalous quartic couplings from events with four leptons and two jets in proton–proton collisions at* $\sqrt{s} = 13$ *TeV*, *Phys. Lett. B* **774** (2017) 682 [1708.02812].

[70] CMS collaboration, *Measurement of differential cross sections for Z boson pair production in association with jets at* $\sqrt{s} = 8$ *and 13 TeV*, *Phys. Lett. B* **789** (2019) 19 [1806.11073].

[71] ATLAS collaboration, *Observation of electroweak* $W^\pm Z$ *boson pair production in association with two jets in pp collisions at* $\sqrt{s} = 13$ *TeV with the ATLAS detector*, *Phys. Lett. B* **793** (2019) 469 [1812.09740].

[72] CMS collaboration, *Measurement of electroweak WZ boson production and search for new physics in WZ + two jets events in pp collisions at* $\sqrt{s} = 13$*TeV*, *Phys. Lett. B* **795** (2019) 281 [1901.04060].

[73] CMS collaboration, *Observation of electroweak production of same-sign W boson pairs in the two jet and two same-sign lepton final state in proton-proton collisions at* $\sqrt{s} = 13$ *TeV*, *Phys. Rev. Lett.* **120** (2018) 081801 [1709.05822].

[74] CMS collaboration, *Search for anomalous electroweak production of vector boson pairs in association with two jets in proton-proton collisions at 13 TeV*, *Phys. Lett. B* **798** (2019) 134985 [1905.07445].

[75] CMS collaboration, *Observation of electroweak production of* $W\gamma$ *with two jets in proton-proton collisions at* $\sqrt{s} = 13$ *TeV*, *Phys. Lett. B* **811** (2020) 135988 [2008.10521].

[76] CMS collaboration, *Measurements of production cross sections of WZ and same-sign WW boson pairs in association with two jets in proton-proton collisions at $\sqrt{s} = 13$ TeV*, *Phys. Lett. B* **809** (2020) 135710 [2005.01173].

[77] CMS collaboration, *Evidence for electroweak production of four charged leptons and two jets in proton-proton collisions at $\sqrt{s} = 13$ TeV*, *Phys. Lett. B* **812** (2021) 135992 [2008.07013].

[78] CMS collaboration, *Measurement of the electroweak production of $Z\gamma$ and two jets in proton-proton collisions at $\sqrt{s} = 13$ TeV and constraints on anomalous quartic gauge couplings*, 2106.11082.

[79] CMS collaboration, *Evidence for exclusive $\gamma\gamma \to W^+W^-$ production and constraints on anomalous quartic gauge couplings in pp collisions at $\sqrt{s} = 7$ and 8 TeV*, *JHEP* **08** (2016) 119 [1604.04464].

[80] M. Rauch, *Vector-Boson Fusion and Vector-Boson Scattering*, 1610.08420.

[81] J. Alwall, R. Frederix, S. Frixione, V. Hirschi, F. Maltoni, O. Mattelaer et al., *The automated computation of tree-level and next-to-leading order differential cross sections, and their matching to parton shower simulations*, *JHEP* **07** (2014) 079 [1405.0301].

[82] N. D. Christensen and C. Duhr, *FeynRules - Feynman rules made easy*, *Comput. Phys. Commun.* **180** (2009) 1614 [0806.4194].

[83] T. Sjöstrand, S. Ask, J. R. Christiansen, R. Corke, N. Desai, P. Ilten et al., *An introduction to PYTHIA 8.2*, *Comput. Phys. Commun.* **191** (2015) 159 [1410.3012].

[84] NNPDF collaboration, *Parton distributions with QED corrections*, *Nucl. Phys. B* **877** (2013) 290 [1308.0598].

[85] DELPHES 3 collaboration, *DELPHES 3, A modular framework for fast simulation of a generic collider experiment*, *JHEP* **02** (2014) 057 [1307.6346].

[86] Y. LeCun, Y. Bengio and G. Hinton, *Deep learning*, *Nature* **521** (2015) 436.

[87] K. He, X. Zhang, S. Ren and J. Sun, *Delving Deep into Rectifiers: Surpassing Human-Level Performance on ImageNet Classification*, 1502.01852.

[88] M. Abadi et al., *TensorFlow: Large-Scale Machine Learning on Heterogeneous Distributed Systems*, 1603.04467.

[89] Y.-C. Guo, F. Feng, A. Di, S.-Q. Lu and J.-C. Yang, *MLAnalysis: An open-source program for high energy physics analyses*, *Comput. Phys. Commun.* **294** (2024) 108957 [2305.00964].

[90] CMS collaboration, *Measurement of the $t\bar{t}$ production cross section using events with one lepton and at least one jet in pp collisions at $\sqrt{s} = 13$ TeV*, *JHEP* **09** (2017) 051 [1701.06228].

[91] ATLAS collaboration, *ATLAS b-jet identification performance and efficiency measurement with $t\bar{t}$ events in pp collisions at $\sqrt{s} = 13$ TeV*, *Eur. Phys. J. C* **79** (2 019) 970 [1907.05120].

[92] J. Kalinowski, P. Kozów, S. Pokorski, J. Rosiek, M. Szleper and S. Tkaczyk, *Same-sign WW scattering at the LHC: can we discover BSM effects before discovering new states?*, *Eur. Phys. J. C* **78** (2018) 403 [1802.02366].

[93] W. Kilian, T. Ohl, J. Reuter and M. Sekulla, *High-Energy Vector Boson Scattering after the Higgs Discovery*, *Phys. Rev. D* **91** (2015) 096007 [1408.6207].

[94] R. L. Delgado, A. Dobado, M. Espada, F. J. Llanes-Estrada and I. L. Merino, *Collider production of electroweak resonances from $\gamma\gamma$ states*, *JHEP* **11** (2018) 010 [1710.07548].

[95] R. L. Delgado, A. Dobado and F. J. Llanes-Estrada, *Coupling WW, ZZ unitarized amplitudes to $\gamma\gamma$ in the TeV region*, *Eur. Phys. J. C* **77** (2017) 205 [1609.06206].

[96] C. Garcia-Garcia, M. Herrero and R. A. Morales, *Unitarization effects in EFT predictions of WZ scattering at the LHC*, *Phys. Rev. D* **100** (2019) 096003 [1907.06668].

[97] M. Jacob and G. Wick, *On the General Theory of Collisions for Particles with Spin*, *Annals Phys.* **7** (1959) 404.

[98] J. Layssac, F. Renard and G. Gounaris, *Unitarity constraints for transverse gauge bosons at LEP and supercolliders*, *Phys. Lett. B* **332** (1994) 146 [hep-ph/9311370].

[99] T. Corbett, O. Éboli and M. Gonzalez-Garcia, *Unitarity Constraints on Dimension-six Operators II: Including Fermionic Operators*, *Phys. Rev. D* **96** (2017) 035006 [1705.09294].

[100] R. Gomez-Ambrosio, *Vector Boson Scattering Studies in CMS: The $pp \to ZZjj$ Channel*, *Acta Phys. Polon. Supp.* **11** (2018) 239 [1807.09634].

[101] E. d. S. Almeida, O. J. P. Éboli and M. C. Gonzalez–Garcia, *Unitarity constraints on anomalous quartic couplings*, *Phys. Rev. D* **101** (2020) 113003 [2004.05174].

[102] W. Kilian, S. Sun, Q.-S. Yan, X. Zhao and Z. Zhao, *Multi-Higgs boson production and unitarity in vector-boson fusion at future hadron colliders*, *Phys. Rev. D* **101** (2020) 076012 [1808.05534].

[103] W. Kilian, S. Sun, Q.-S. Yan, X. Zhao and Z. Zhao, *Highly Boosted Higgs Bosons and Unitarity in Vector-Boson Fusion at Future Hadron Colliders*, *JHEP* **05** (2021) 198 [2101.12537].

[104] D. Barducci et al., *Interpreting top-quark LHC measurements in the standard-model effective field theory*, 1802.07237.

[105] D. Racco, A. Wulzer and F. Zwirner, *Robust collider limits on heavy-mediator Dark Matter*, *JHEP* **05** (2015) 009 [1502.04701].

[106] M. Szleper, G. Chaudhary, J. Kalinowski, M. Kaur, P. Kozow, S. Pokorski et al., *EFT validity issues in Vector Boson Scattering processes*, *PoS* **LHCP2020** (2021) 023.

[107] ATLAS collaboration, *Search for high-mass dilepton resonances using 139 fb^{-1} of pp collision data collected at $\sqrt{s}$ =13 TeV with the ATLAS detector*, *Phys. Lett. B* **796** (2019) 68 [1903.06248].

[108] D. Liu, C. Sun and J. Gao, *Constraints on neutrino non-standard interactions from LHC data with large missing transverse momentum*, *JHEP* **02** (2021) 033 [2009.06668].

[109] ATLAS, CMS collaboration, *Electroweak measurements at High-Luminosity LHC*, *PoS* **LHCP2019** (2019) 242.

[110] P. Kozów, L. Merlo, S. Pokorski and M. Szleper, *Same-sign WW Scattering in the HEFT: Discoverability vs. EFT Validity*, *JHEP* **07** (2019) 021 [1905.03354].